Geoscience Frontiers 7 (2016) 591–607

HOSTED BY

Contents lists available at ScienceDirect

China University of Geosciences (Beijing)

Geoscience Frontiers

journal homepage: www.elsevier.com/locate/gsf

Research paper

Quantifying geological uncertainty in metamorphic phase equilibria modelling; a Monte Carlo assessment and implications for tectonic interpretations

Richard M. Palin [a,*], Owen M. Weller [b], David J. Waters [c], Brendan Dyck [c]

[a] Institute of Geosciences, Johannes-Gutenberg University Mainz, 55128, Mainz, Germany
[b] Geological Survey of Canada, 601 Booth Street, Ottawa, ON, K1A 0E8, Canada
[c] Department of Earth Sciences, University of Oxford, Oxford, OX1 3AN, United Kingdom

ARTICLE INFO

Article history:
Received 19 June 2015
Received in revised form
21 August 2015
Accepted 26 August 2015
Available online 25 September 2015

Keywords:
Geological uncertainty
Error
Pseudosection
Monte Carlo
MnNCKFMASHTO

ABSTRACT

Pseudosection modelling is rapidly becoming an essential part of a petrologist's toolkit and often forms the basis of interpreting the tectonothermal evolution of a rock sample, outcrop, or geological region. Of the several factors that can affect the accuracy and precision of such calculated phase diagrams, "geological" uncertainty related to natural petrographic variation at the hand sample- and/or thin section-scale is rarely considered. Such uncertainty influences the sample's bulk composition, which is the primary control on its equilibrium phase relationships and thus the interpreted pressure–temperature (*P–T*) conditions of formation. Two case study examples—a garnet–cordierite granofels and a garnet–staurolite–kyanite schist—are used to compare the relative importance that geological uncertainty has on bulk compositions determined via (1) X-ray fluorescence (XRF) or (2) point counting techniques. We show that only minor mineralogical variation at the thin-section scale propagates through the phase equilibria modelling procedure and affects the absolute *P–T* conditions at which key assemblages are stable. Absolute displacements of equilibria can approach ±1 kbar for only a moderate degree of modal proportion uncertainty, thus being essentially similar to the magnitudes reported for analytical uncertainties in conventional thermobarometry. Bulk compositions determined from multiple thin sections of a heterogeneous garnet–staurolite–kyanite schist show a wide range in major-element oxides, owing to notable variation in mineral proportions. Pseudosections constructed for individual point count-derived bulks accurately reproduce this variability on a case-by-case basis, though averaged proportions do not correlate with those calculated at equivalent peak *P–T* conditions for a whole-rock XRF-derived bulk composition. The main discrepancies relate to varying proportions of matrix phases (primarily mica) relative to porphyroblasts (primarily staurolite and kyanite), indicating that point counting preserves small-scale petrographic features that are otherwise averaged out in XRF analysis of a larger sample. Careful consideration of the size of the equilibration volume, the constituents that comprise the effective bulk composition, and the best technique to employ for its determination based on rock type and petrographic character, offer the best chance to produce trustworthy data from pseudosection analysis.

1. Introduction

An equilibrium model of metamorphism, where the mineral assemblage developed in a rock is a combined function of the bulk chemical composition (*X*) of the equilibration volume and the prevailing pressure–temperature (*P–T*) conditions at the time of crystallisation (Khorzhinskii, 1959; Thompson, 1959; Powell et al., 1998; Guiraud et al., 2001), has been widely adopted by the modern geological community. Indeed, this model allows the use of forward or reverse petrological modelling to characterise the relative or absolute changes in *P–T–X* conditions experienced by a rock, for example, during orogenesis. The compilation and

* Corresponding author.
E-mail address: richardmpalin@gmail.com (R.M. Palin).
Peer-review under responsibility of China University of Geosciences (Beijing).

http://dx.doi.org/10.1016/j.gsf.2015.08.005

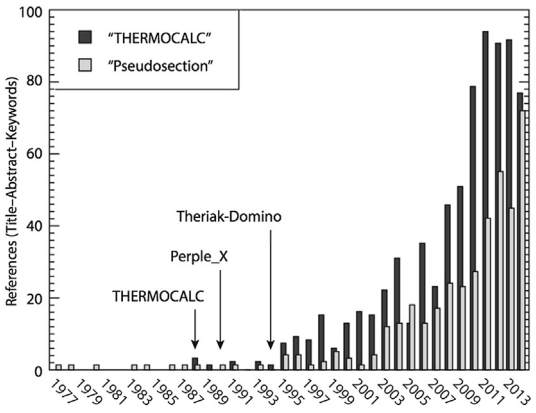

Figure 1. Bar chart highlighting the rapid and recent increases in peer-reviewed research articles published in ISI-indexed journals with the term "pseudosection" or "THERMOCALC" in the article title, abstract, or keywords in the physical sciences subject area. Data were obtained from the Scopus® online database. Bottom axis represents publication year.

expansion of internally-consistent thermodynamic datasets relevant to petrologists (e.g. Helgeson et al., 1978; Berman, 1988; Holland and Powell, 1998, 2011) and the advent of associated computer software capable of manipulating this information to the user's requirements (e.g. thermocalc – Powell and Holland, 1988; Perple_X – Connolly, 1990; Theriak-Domino – De Capitani, 1994) has led to phase diagram modelling—the graphical representation of equilibrium relations between mineral and fluid species over a range of P–T–X space—being increasingly relied upon to make detailed quantitative analysis of the tectonothermal evolution of geological terranes (e.g. Vance and Mahar, 1998; Hoschek, 2004; Štípská and Powell, 2005; Caddick et al., 2007; Palin et al., 2012, 2013a; St-Onge et al., 2013; Mottram et al., 2014; Pownall et al., 2014; Dyck et al., 2015; Weller et al., 2015a,b). Evidence for this trend is given by the number of research articles published in ISI-indexed journals that use the term "pseudosection" (a phase diagram showing equilibrium phase assemblage relations for a specific bulk-rock composition as a function of two independent extensive variables; commonly P and T) or "thermocalc" in the article title, abstract, or keywords, which has shown a notable increase in recent years (Fig. 1).[1] As the quality and quantity of thermodynamic data and activity–composition (a–x) relations for phases of interest continues to improve, this technique will assume an increasingly important role in petrological investigations and geodynamic interpretations. Thus, it is essential that the relative magnitudes of the various associated uncertainties are quantified and well understood.

Phase diagram modelling is invariably affected by both systematic and random errors. Systematic errors mostly relate to (1) uncertainties on the physical properties of end-members in thermodynamic datasets and (2) uncertainties associated with the formulation of a–x relations describing the thermodynamic properties of solid solution mixing of end-members within one phase (e.g. Evans, 2004; Evans and Bickle, 2005; Green et al., 2013). As such errors are applied equally to all calculations, the relative differences between each result should be small if the same thermodynamic dataset and a–x relations are used within (or between) studies (Worley and Powell, 2000). Consequently, studies do not generally report the magnitude of this propagated uncertainty on their calculated phase diagrams, nor discuss the potential influence of such uncertainty on the interpretation of their results (though, see Fig. 7b in Angiboust et al., 2011 and Fig. 10c in Palin et al., 2012 for exceptions). By contrast, random sources of uncertainty have errors that vary according to each analysis, thus affecting the relative precision of different results. In the context of phase equilibria modelling, the two main sources are (1) analytical (or "machine") error relating to the imprecision of measurement of mineral and/or rock compositions and (2) geological error, which is taken here to comprise non-analytical procedures involved in a petrological investigation (e.g. bias in sampling techniques or petrographic interpretation of the degree of equilibrium). While the effects of propagating systematic errors and random analytical uncertainties on measured mineral compositions through thermodynamic calculations are well understood (Hodges and McKenna, 1987; Kohn and Spear, 1991; Powell and Holland, 1994, 2008), we are unaware of any attempts to directly assess the equivalent importance of geological errors on the pseudosection modelling process.

The influence of such geological error can be envisaged via a hypothetical scenario where a single rock is collected from outcrop, divided into several pieces, and each portion given to a different geologist in order for them to quantify its tectonothermal evolution via pseudosection modelling (Fig. 2). If each geologist uses the same internally consistent thermodynamic dataset and a–x relations for their calculations, then any associated errors with these data or formulations would be applied consistently to each pseudosection. This would affect the overall *accuracy* of the calculated diagrams, but in a systematic fashion (e.g. particular phase assemblage fields may exhibit a common bias to high- or low-T). However, despite being separated from the same parent sample, which has a definite and measurable bulk composition, petrological differences (e.g. varying mineral abundances) between each rock portion would cause their measured (or calculated) bulk compositions to differ (Fig. 2). As bulk-rock composition is the primary control on pseudosection topology (Stüwe, 1997), such random geological errors would affect the relative *precision* of each calculated phase diagram and so the P–T–X conditions over which the interpreted equilibrium mineral assemblage is stable would likely vary for each geologist in a non-systematic manner.

This thought experiment raises important questions about the reliability of results commonly obtained via phase equilibria modelling. Exactly how different would the calculated P–T conditions of prograde, peak, and/or retrograde metamorphism be if the bulk-rock composition were determined using different techniques? Would this produce a significant difference in the interpreted tectonic evolutions, or is the magnitude of geological error simply too small for it to be considered in the phase diagram modelling process? In this contribution, we investigate these issues with two case study examples: a low-P contact-metamorphosed granofels from the Odenwald Crystalline Complex, central Germany, and a regionally-metamorphosed medium-P amphibolite-facies schist from the Danba Structural Culmination, eastern Tibet, placing particular emphasis on the different techniques used to determine the bulk composition of a rock sample. For the former lithology, we determine how uncertainties associated with point-counted mineral proportions propagate through to pseudosection-derived calculated P–T conditions by using a Monte Carlo method documented recently by Palin et al. (2014a). For the latter, we examine how petrographic variability occurring between different thin sections of the same rock compares with a volume-integrated bulk-rock composition obtained via X-ray fluorescence (XRF), and the differences that this variability imparts on calculated phase

[1] Although these trends are non-normalised and do not account for increases in the total number of research articles published annually as new journals emerge, general consensus in the metamorphic geology community is that phase equilibria modelling has become a significantly more important research tool in recent years.

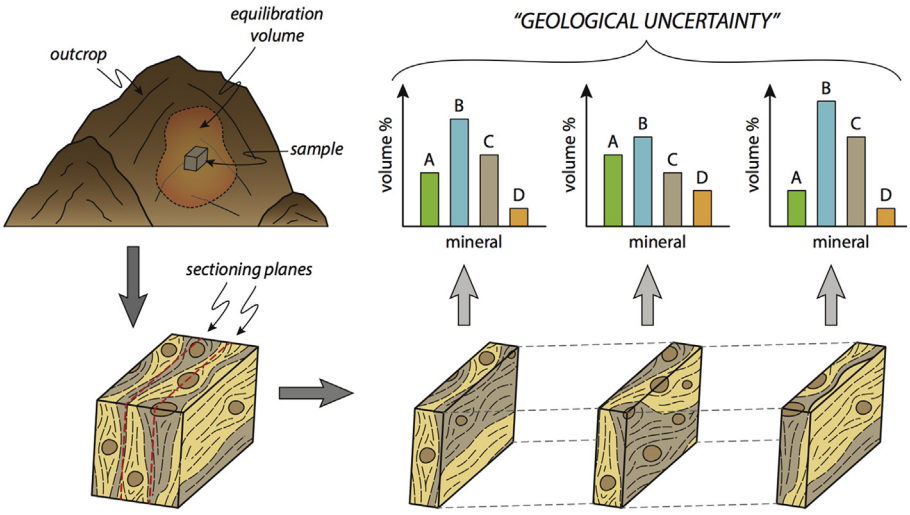

Figure 2. Sketch illustration of the source of geological uncertainty investigated in this work that stems from petrological variation on the hand sample- and thin section scale.

equilibria. An Excel spreadsheet that can be used for executing the Monte Carlo randomisation procedure described herein is also provided as a downloadable file.

2. Bulk composition determination

The process of obtaining a suitable bulk-rock composition as a starting point for pseudosection construction is non-trivial, as the bulk composition of a rock sample can be determined—and subsequently simplified—in various ways (Robinson, 1991). The two main methods described in the literature to obtain bulk-rock compositions utilise either whole-rock XRF analyses (hereafter, XRF-derived) or proportions of minerals coupled with their individual representative compositions (hereafter, point count-derived). Each of these techniques has various advantages and shortcomings, and it is often the case that one method is more suited to a particular rock type and/or geological scenario than the other.

XRF provides a full elemental analysis (for those heavier than Na) of a sample and so produces a *total* bulk composition for the rock in question (Fig. 3a), though this technique cannot distinguish between different ionic valence states and so cannot determine the relative proportions of FeO and Fe_2O_3 (i.e. $X_{Fe^{3+}}$ = molar Fe^{3+}/total Fe). Commonly, the oxidation state of a rock can be estimated to within a broad range based on the accessory Fe–Ti oxide minerals present (Chinner, 1960; Diener et al., 2007), or else wet chemistry/titration can be additionally performed in order to provide a maximum constraint on bulk-rock $X_{Fe^{3+}}$ (e.g. Phillips et al., 2008; Plumhoff et al., 2015). The analysed proportions of oxide components in XRF-derived total bulk compositions often contain contributions from minerals that cannot be readily reproduced during phase equilibria modelling due to a lack of suitable end-member thermodynamic data or a–x relations for solid-solution behaviour, such as Ca from apatite, Al from tourmaline, Fe from pyrite etc; however, if the proportions of the minerals providing these unwanted contributions can be determined, corrections can be made to the actual bulk composition in order to produce a *model-ready* bulk composition. For example, a molar amount of CaO equal to 3.33-times that of P_2O_5 can be subtracted from the XRF-derived actual bulk composition to account for the presence of apatite, assuming that it is the sole phosphorus-bearing mineral (e.g. Pitra and De Waal, 2001; Weller et al., 2015a). Effective usage of XRF requires that the size of the sample analysed is smaller than the volume of equilibration for the metamorphic event being investigated (cf. Fig. 3a).

In contrast to XRF analysis, a representative bulk-rock composition may be obtained via a weighted calculation involving the proportions of minerals present in a thin section and their representative compositions (e.g. Carson et al., 1999; Indares et al., 2008). Here, as the geologist decides which minerals to include in this calculation, the total bulk composition is immediately reduced to a model-ready bulk composition by disregarding phases containing components outside of the chosen model system (Fig. 3b). Indeed, standalone programs/worksheets have been created with the explicit purpose of aiding these choices and automating the calculation procedure (e.g. RockMaker: Büttner, 2012). This method of bulk composition determination is essential for rocks exhibiting mosaic equilibrium (Powell, 1978) or those showing clear textural evidence for polymetamorphism (Argles et al., 1999). In these cases, individual domains judged on various petrological criteria to be out of equilibrium with the larger reacting volume (e.g. garnet cores) can be excluded from the bulk composition contribution (St-Onge et al., 2013). Thus, even though some minerals may be reproducible in a model, if they are part of a domain that is outside of the equilibration volume, they are excluded from the model-ready bulk

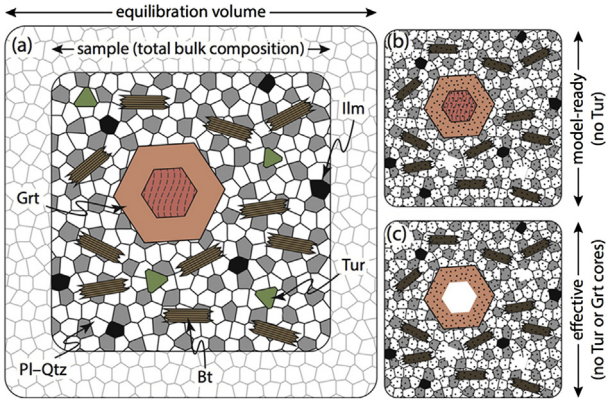

Figure 3. Graphical definitions of various bulk composition nomenclature commonly used in the literature. See main text for discussion. Note that while minerals such as tourmaline that contain components outside of the model system chosen for phase equilibria modelling may form part of the effective bulk composition, they are not treated as such for modelling purposes.

composition, thus producing an *effective* bulk composition (Fig. 3c). This method also allows the compositions and proportions of phases calculated via pseudosection modelling to be compared directly to those in the thin section of interest, thus often providing further constraints on interpreted *P*–*T* conditions of metamorphism (e.g. Pearce et al., 2015). Adjustments to mineral compositions obtained via electron microprobe analyses must commonly be made in order to account for system components that do not fully correlate with the *a*–*x* relations being utilised. These can involve components that are considered in the bulk-rock model system, but not within the *a*–*x* relation for the phase of interest (e.g. K and Ti in amphibole: Diener and Powell, 2012), or to accommodate crystallographic constraints, such as the current mica models requiring a full interlayer site (White, R.W. et al., 2014a) despite electron microprobe analyses invariably reporting vacancies (Waters and Charnley, 2002), whether real or apparent. Such corrections to mineral compositions form the basis of the 'ideal analysis' concept of Powell and Holland (2008), which is employed in our investigation for point count-derived bulk composition calculations. For a more detailed description of the ideal analysis technique, the reader is referred to Appendix 1 of Powell and Holland (2008).

Although the latter technique described above superficially appears to provide the most suitable bulk-rock composition for pseudosection construction, geological procedures involved in rock collection, point counting, and petrographic investigation can unwittingly introduce bias. For example, in porphyroblast-bearing lithologies, are all thin sections broadly representative of the rock from which they are cut (cf. Fig. 2)? Rocks containing garnet often provide the best chance of constraining the tectonothermal history of a region owing to its versatility in preserving *P*–*T*-dependent inclusion suites and major and rare earth element compositional zoning profiles (Caddick et al., 2010; Baxter et al., 2013; Palin et al., 2014b; Wilke et al., 2015). It is natural, therefore, that a geologist will endeavour to have the largest garnets exposed within the thin section area, as these have best chance of preserving early prograde history in high-grade rocks; but what if garnet is only a minor constituent and comprises <1 vol.% of the rock? Here, a thin section area analysis would almost certainly overestimate its proportion for the rock as a whole, and potentially even for the local equilibrium domain. This issue is compounded by the uncertainty of whether the interior of a garnet is in complete chemical communication with the matrix, although complexities involving progressive cation fractionation into growing porphyroblasts (Marmo et al., 2002) lie outside of the scope of this investigation. Evans and Bickle (2005) briefly discussed these issues and suggested that the most reliable bulk composition that can be obtained for modelling "*lies somewhere between the thin section-scale point count-derived composition and the hand sample-scale XRF-derived composition*". In the case-study examples below, we directly investigate this issue in greater detail.

3. Case study 1: Garnet–Cordierite granofels

In order to assess the sensitivity of calculated assemblage field boundaries in *P*–*T* space to variations in point count-derived bulk compositions related to uncertainty in the calculation of mineral modal proportions (Hirsch, 2012), pseudosections were constructed for a contact-metamorphosed garnet- and cordierite-bearing granofels from the Odenwald Crystalline Complex of the Mid-German Crystalline Rise; a NE–SW-trending zone of late Palaeozoic high-grade metamorphic and magmatic lithologies that formed during the assembly of Pangaea (Matte, 2001). The Odenwald Crystalline Complex contains abundant gabbroic, granodioritic, and granitic plutons and subordinate low-*P*, medium/high-*T* contact-metamorphosed volcanic and sedimentary sequences (Krohe, 1991; Okrusch, 1995; Stein and Dietl, 2001; Will and Schmädicke, 2003; Will et al., 2015). The variable occurrence of andalusite, sillimanite, and/or cordierite in metapelites from the centre of the Complex, coupled with the general absence of partial melting, has been previously used to infer peak *P*–*T* conditions of ~3–5 kbar and ~600–700 °C (Willner et al., 1991; Okrusch, 1995; Will and Schmädicke, 2003).

3.1. Sample petrography and bulk compositions

Sample OD68-12 contains abundant garnet porphyroblasts in a cordierite–plagioclase–biotite-dominated matrix, alongside minor quartz, sillimanite, and ilmenite (Fig. 4a). Accessory apatite, monazite, zircon, tourmaline, and pyrite also occur. Garnet porphyroblasts are typically subhedral, up to 3 mm in diameter, and show concentric compositional zoning profiles: broad cores are compositionally homogenous ($Alm_{68–73}Prp_{18–22}Grs_{5–6}Sps_{4–5}$) and are surrounded by extremely thin rim regions that are relatively enriched in Fe and Mn, and depleted in Mg and Ca ($Alm_{79}Prp_{10}Grs_{4}Sps_{7}$; Fig. 4b). This coupled increase in Mn-content and decrease in X_{Mg} (= Mg/(Fe + Mg)) at rims is typical of retrograde diffusional cation exchange with matrix minerals (Kohn and

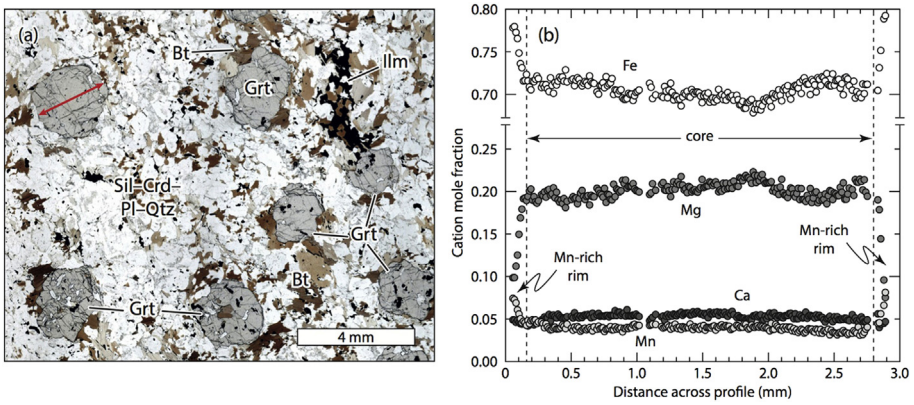

Figure 4. Petrography of sample OD68-12. (a) Plane-polarised light photomicrograph showing the granofelsic texture of sample OD68-12. Subhedral garnet porphyroblasts occur in a matrix comprised mainly of cordierite, plagioclase, and biotite, with proportionally minor quartz, sillimanite, and ilmenite. Red arrow indicates the position of the garnet compositional line profile shown in Fig. 4b. (b) Garnet compositional line profile running from rim to rim. The line profile is non-continuous where the analytical traverse crosses inclusions and fractures, analyses of which are omitted.

Table 1
Representative mineral compositional analyses from sample OD68-12. Idealisation of each individual mineral composition follows the procedures outlined in Appendix 1 of Powell and Holland (2008).

	Electron microprobe-derived composition						"Ideal analysis"					
Mineral	Bt	Crd	Grt	Grt	Ilm	Pl	Bt	Crd	Grt	Grt	Ilm	Pl
Location	Matrix	Matrix	Core	Rim	Matrix	Matrix	Matrix	Matrix	Core	Rim	Matrix	Matrix
SiO_2	34.60	47.84	37.09	36.57	0.09	55.25	-	-	-	-	-	-
TiO_2	2.83	0.00	0.27	0.10	53.63	0.00	-	-	-	-	-	-
Al_2O_3	19.06	32.64	20.89	20.45	0.09	27.63	-	-	-	-	-	-
Fe_2O_3	0.00	0.00	1.11	1.69	0.00	0.01	-	-	-	-	-	-
FeO	21.13	9.84	31.50	32.95	45.68	0.00	-	-	-	-	-	-
MnO	0.09	0.21	1.92	2.89	0.95	0.00	-	-	-	-	-	-
MgO	7.91	6.89	4.86	3.27	0.14	0.00	-	-	-	-	-	-
CaO	0.07	0.00	1.94	1.65	0.02	10.13	-	-	-	-	-	-
Na_2O	0.00	0.00	0.00	0.00	0.00	5.09	-	-	-	-	-	-
K_2O	9.48	0.01	0.00	0.00	0.00	0.11	-	-	-	-	-	-
Total	95.17	97.43	99.58	99.57	100.60	98.22	-	-	-	-	-	-
Si	2.66	5.00	2.97	2.96	0.00	2.52	2.67	5.00	3.00	3.00	-	2.51
Ti	0.16	0.00	0.02	0.01	1.01	0.00	0.16	-	-	-	1.02	-
Al	1.73	4.02	1.97	1.95	0.00	1.50	1.73	4.00	2.00	2.00	-	1.49
Fe^{3+}	0.00	0.00	0.07	0.10	0.00	0.00	0.15	-	-	-	0.00	-
Fe^{2+}	1.36	0.86	2.11	2.23	0.96	0.00	1.21	0.90	2.11	2.24	0.96	-
Mn	0.01	0.02	0.13	0.20	0.02	0.00	0.01	0.02	0.13	0.20	0.02	-
Mg	0.91	1.07	0.58	0.40	0.01	0.00	0.91	1.08	0.58	0.40	0.00	-
Ca	0.01	0.00	0.17	0.14	0.00	0.51	-	-	0.17	0.14	-	0.49
Na	0.00	0.00	0.00	0.00	0.00	0.47	-	-	-	-	-	0.51
K	0.93	0.00	0.00	0.00	0.00	0.01	1.00	-	-	-	-	0.01
Sum	7.77	10.98	8.00	7.99	2.00	5.00	7.84	11.00	8.00	8.00	2.00	5.00
Oxygen	11	18	12	12	3	8	11	18	12	12	3	8
X_{Mg}	0.40	0.56	0.22	0.15	-	-	0.43	0.55	0.22	0.15	-	-
Alm	-	-	0.71	0.75	-	-	-	-	0.70	0.75	-	-
Prp	-	-	0.19	0.13	-	-	-	-	0.19	0.13	-	-
Grs	-	-	0.06	0.05	-	-	-	-	0.06	0.05	-	-
Sps	-	-	0.04	0.07	-	-	-	-	0.04	0.07	-	-
X_{An}	-	-	-	-	-	0.51	-	-	-	-	-	0.49

$X_{An} = Ca/(Ca + Na + K)$.

Spear, 2000). Biotite in the matrix and grains adjacent to garnet outer rims have similar compositions, with an X_{Mg} range of 0.39–0.41 and Ti content of 0.13–0.16 cpfu (Table 1). Cordierite has $X_{Mg} = 0.53–0.56$ and plagioclase feldspar has an anorthite content ($X_{An} = Ca/(Ca + Na + K)$) of 0.51–0.52 (Table 1), with both minerals lacking systematic internal compositional zoning.

The absence of compositional variation between grains, or zoning within individual minerals (with the exception of garnet outer rims), in sample OD68-12 is conducive to a point count-derived bulk composition being calculated. Volume proportions of minerals were determined using the software JMicroVision (Roduit, 2010), with each individual count consisting of five hundred points randomly distributed over a digitally scanned thin-section image. Average proportions obtained from three separate thin sections are as follows: 11.1% garnet, 35.9% cordierite, 17.4% biotite, 32.0% plagioclase, 0.8% ilmenite, 0.8% sillimanite, and 2.0% quartz (Table 2). No significant variation was noted between each thin section, likely owing to the relatively fine-grained and texturally isotropic nature of the sample. Mineral compositional data were obtained at the Department of Earth Sciences, University of Oxford, UK, using the techniques and machine operating conditions described in Palin et al. (2013b). Representative electron microprobe-derived compositions were idealised before being combined with their individual proportions for bulk-composition calculation (cf. Appendix 1 in Powell and Holland, 2008) and are shown in Table 1. The contribution by garnet was constructed via the summation of concentric shells, assuming a spherical geometry. The calculated H_2O content assumed stochiometric proportions within each hydrous phase and the ferric iron content, where relevant, was determined by charge-balance calculations. The resultant bulk composition for sample OD68-12 in the MnNCKFMASHTO ($MnO–Na_2O–CaO–K_2O–FeO–MgO–Al_2O_3–SiO_2–H_2O–TiO_2–O_2$) model system is: H_2O–3.53; SiO_2–51.65; Al_2O–16.96; CaO–3.89; MgO–7.51; FeO–12.02; K_2O–1.35; Na_2O–1.85; TiO_2–1.02; MnO–0.36; O_2–0.20 (mol.% oxides). A worked example of this bulk composition calculation is given in an Excel spreadsheet that is available for download as an electronic attachment to this work. A description of the setup conditions and $a–x$ relations used for modelling is given in Appendix A, and all mineral abbreviations are after Kretz (1983).

3.2. Initial results

A calculated $P–T$ pseudosection for the OD68-12 point count-derived bulk composition is shown in Fig. 5. Importantly, Powell et al. (2005) noted that it is the preserved mineral assemblage – and in some cases also their individual proportions – that is most suitable for determining peak metamorphic conditions in high-grade rocks via pseudosection modelling, rather than mineral compositions, which are more readily affected by retrograde diffusion-related processes. Consequently, we focus our sample-specific interpretations and subsequent discussions on the sensitivity of the extent and position of the peak assemblage field and modal proportion contours in $P–T$ space, acknowledging that the associated mineral compositions that are expected at those conditions may not provide a perfect match to those in the sample due to retrograde change. Modal proportions of phases reported from

Table 2
Perturbed phase proportions and recalculated bulk compositions for sample OD68-12.

Randomization no.	%[a]	Non-normalized perturbed mineral proportions							Normalized perturbed mineral proportions							Bulk composition (mol.% oxides)										
		Grt	Crd	Bt	Pl	Ilm	Sil	Qtz	Grt	Crd	Bt	Pl	Ilm	Sil	Qtz	H_2O	SiO_2	Al_2O_3	CaO	MgO	FeO	K_2O	Na_2O	TiO_2	MnO	O
1	10	10.27	33.95	20.80	30.62	0.83	0.74	2.13	10.34	34.17	20.94	30.83	0.83	0.74	2.14	3.96	50.77	16.81	3.68	7.61	12.14	1.59	1.75	1.12	0.34	0.24
2	10	12.44	32.63	17.46	29.56	0.64	0.83	2.31	12.98	34.03	18.21	30.83	0.67	0.87	2.41	3.53	51.20	16.90	3.73	7.48	12.50	1.38	1.74	0.93	0.39	0.20
3	10	10.83	38.95	14.06	33.65	0.75	0.90	1.87	10.72	38.56	13.92	33.32	0.74	0.89	1.85	3.06	52.30	17.57	4.02	7.26	11.36	1.09	1.93	0.90	0.36	0.16
4	10	12.72	33.71	18.83	36.81	0.94	0.68	2.19	12.01	31.84	17.79	34.76	0.89	0.64	2.07	3.43	51.42	16.87	4.15	7.12	12.02	1.36	1.98	1.08	0.37	0.20
5	10	9.95	35.40	17.93	32.27	0.86	0.69	2.12	10.03	35.69	18.07	32.52	0.86	0.69	2.14	3.60	51.52	17.06	3.88	7.40	11.66	1.39	1.87	1.08	0.34	0.20
6	10	11.44	35.45	14.05	35.54	0.72	0.98	2.00	11.42	35.39	14.03	35.48	0.72	0.98	2.00	2.99	52.44	17.44	4.27	7.00	11.34	1.09	2.04	0.87	0.36	0.16
7	10	9.64	35.33	16.26	29.69	0.80	0.99	2.06	10.17	37.28	17.16	31.33	0.84	1.04	2.18	3.50	51.61	17.27	3.76	7.47	11.68	1.32	1.80	1.04	0.34	0.19
8	10	12.23	36.44	17.11	35.68	0.77	0.91	1.97	11.64	34.66	16.28	33.95	0.73	0.87	1.88	3.29	51.74	17.22	4.08	7.21	11.77	1.25	1.94	0.93	0.37	0.18
9	10	9.86	37.30	18.43	38.27	0.64	0.63	2.21	9.18	34.75	17.17	35.65	0.60	0.59	2.06	3.47	52.25	17.21	4.24	7.13	10.94	1.34	2.06	0.87	0.31	0.20
10	10	12.15	41.62	15.96	31.24	0.80	0.82	2.22	11.59	39.71	15.22	29.81	0.77	0.79	2.11	3.27	51.73	17.37	3.63	7.61	12.03	1.17	1.71	0.94	0.38	0.17
Mean		**11.15**	**36.08**	**17.09**	**33.33**	**0.77**	**0.82**	**2.11**	**11.01**	**35.61**	**16.88**	**32.85**	**0.77**	**0.81**	**2.08**	**3.41**	**51.70**	**17.17**	**3.94**	**7.33**	**11.74**	**1.30**	**1.88**	**0.98**	**0.36**	**0.19**
2 S.D.		2.37	5.33	4.21	6.23	0.18	0.26	0.27	2.24	4.66	4.25	4.20	0.18	0.29	0.32	0.56	1.04	0.51	0.48	0.43	0.91	0.31	0.25	0.19	0.05	0.05
Range		3.07	8.99	6.75	8.71	0.30	0.36	0.44	3.80	7.87	7.02	5.85	0.29	0.45	0.56	0.97	1.67	0.76	0.64	0.61	1.56	0.50	0.35	0.25	0.08	0.08
11	20	7.99	34.83	23.76	33.95	0.90	0.74	1.63	7.70	33.56	22.89	32.70	0.86	0.72	1.57	4.28	50.60	16.86	3.83	7.56	11.49	1.76	1.88	1.20	0.28	0.26
12	20	10.30	28.36	15.75	27.60	1.01	1.04	2.47	11.91	32.78	18.20	31.89	1.17	1.21	2.85	3.50	51.25	16.81	3.82	7.24	12.30	1.38	1.81	1.29	0.37	0.20
13	20	10.10	29.62	14.63	41.07	0.82	0.79	2.55	10.14	29.74	14.69	41.24	0.82	0.79	2.57	2.96	53.14	17.12	4.88	6.37	10.54	1.15	2.38	0.97	0.32	0.17
14	20	9.31	37.11	18.40	28.48	0.57	0.95	1.74	9.64	38.43	19.06	29.50	0.59	0.98	1.80	3.82	51.17	17.30	3.54	7.79	11.77	1.47	1.69	0.90	0.33	0.22
15	20	11.94	36.58	18.85	34.40	0.73	0.90	1.39	11.39	34.92	17.99	32.83	0.70	0.86	1.32	3.55	51.11	17.22	3.94	7.43	11.99	1.38	1.87	0.95	0.36	0.20
16	20	8.03	38.09	20.46	33.70	0.79	0.91	2.14	7.71	36.58	19.65	32.37	0.76	0.88	2.06	3.89	51.54	17.18	3.83	7.50	11.10	1.52	1.87	1.05	0.29	0.22
17	20	11.19	25.21	15.89	19.50	0.86	1.09	1.89	14.80	33.33	21.01	25.78	1.13	1.44	2.50	3.86	49.68	16.61	3.18	7.86	13.84	1.56	1.43	1.31	0.44	0.23
18	20	13.18	31.26	12.02	28.94	0.73	0.61	1.94	14.87	35.25	13.55	32.63	0.82	0.69	2.18	2.87	51.82	17.15	3.99	7.21	12.56	1.04	1.85	0.93	0.44	0.15
19	20	10.16	45.23	15.45	30.80	0.72	0.86	2.16	9.64	42.92	14.66	29.23	0.69	0.81	2.05	3.30	52.11	17.65	3.55	7.73	11.44	1.14	1.70	0.88	0.34	0.17
20	20	14.43	37.75	14.88	29.82	0.97	0.87	2.41	14.27	37.33	14.71	29.49	0.95	0.86	2.38	3.09	51.41	17.12	3.63	7.51	12.81	1.12	1.67	1.05	0.43	0.16
Mean		**10.66**	**34.40**	**17.01**	**30.82**	**0.81**	**0.88**	**2.03**	**11.21**	**35.48**	**17.64**	**31.77**	**0.85**	**0.92**	**2.13**	**3.51**	**51.38**	**17.10**	**3.82**	**7.42**	**11.98**	**1.35**	**1.82**	**1.05**	**0.36**	**0.20**
2 S.D.		4.17	11.70	6.77	11.25	0.26	0.28	0.77	5.45	7.23	6.26	8.04	0.38	0.46	0.94	0.92	1.82	0.58	0.89	0.85	1.89	0.47	0.48	0.32	0.12	0.07
Range		6.44	20.02	11.74	21.58	0.44	0.48	1.17	7.17	13.18	9.34	15.46	0.58	0.75	1.53	1.41	3.46	1.04	1.70	1.49	3.30	0.72	0.95	0.43	0.16	0.11
Original		**11.1**	**35.9**	**17.4**	**32.0**	**0.8**	**0.8**	**2.0**	**11.1**	**35.9**	**17.4**	**32.0**	**0.8**	**0.8**	**2.0**	**3.53**	**51.65**	**16.96**	**3.89**	**7.51**	**12.02**	**1.35**	**1.85**	**1.02**	**0.36**	**0.20**

[a] Percentage threshold by which original modal proportion values were perturbed.

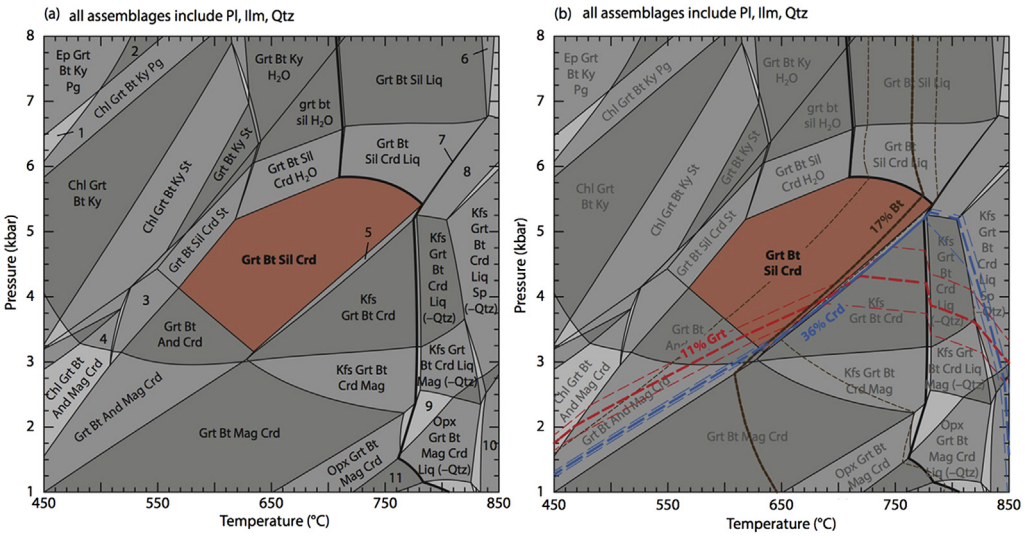

Figure 5. *P–T* pseudosection calculated for sample OD68-12 using an effective bulk composition derived via point counting, as discussed in the main text. Assemblage fields are shaded according to the number of degrees of freedom, with higher-variance assemblages represented by darker shading. (a) Pseudosection showing labelled assemblage fields. The interpreted peak metamorphic assemblage field is shaded in red and labelled with bold text. Heavy line represents the solidus. Numbered fields are as follows: 1 – Ep Grt Bt Ky Pg Chl; 2 – Grt Bt Ky Pg; 3 – Grt Bt And Crd St; 4 – Chl Grt Bt And Crd; 5 – Grt Bt Sil Crd Kfs; 6 – Grt Bt Sil Liq Kfs; 7 – Grt Bt Sil Crd Liq Kfs; 8 – Grt Bt Crd Liq Kfs; 9 – Kfs Grt Bt Crd Liq Mag Opx (–Qtz); 10 – Opx Grt Bt Mag Spl Liq (–Qtz). (b) Pseudosection from part (a) with modal proportion contours for integer-rounded values of the average observed proportions of major minerals garnet (11%), cordierite (36%), and biotite (17%). Percentage labels refer to thick central dashed lines in each contour set, with lighter, dashed, sub-parallel contours representing a proportion ±1% of the observed value. Heavy line represents the solidus.

calculations are determined on a 1-oxygen basis, which provides a reasonable proxy for volume proportions, although minor discrepancies may occur between minerals that have significantly different molar volumes.

The interpreted peak assemblage Grt–Bt–Crd–Sil–Pl–Ilm–Qtz is calculated to occur between 3.25–5.75 kbar and 570–780 °C (Fig. 5a). With increasing temperature, sillimanite becomes unstable and K-feldspar appears, and at lower-pressure conditions andalusite replaces sillimanite as the stable aluminosilicate polymorph. Further refinement of interpreted peak *P–T* conditions within this range can be performed by contouring the calculated pseudosection for modal proportions of major *P–T*-sensitive phases; in this case, garnet, biotite, and cordierite, which were observed to constitute ~11%, ~17%, and ~36% of sample OD68-12, respectively (Table 2). Isomode contours for each of these proportions are shown on Fig. 5b as heavy, dashed lines, with contours representing ±1% of each of these observed values shown as light, sub-parallel, dashed lines in order to illustrate the representative rate of modal proportion change across different assemblage fields. All of these major mineral isomode contours converge at ~3.5–4.0 kbar and ~650–700 °C, at the high-*T*–low-*P* boundary of the peak assemblage field marked by the loss of sillimanite and stabilisation of K-feldspar. Although analysed mineral compositions from peak phases may not necessarily correlate well with calculated values at high-grade conditions as noted above, isopleths representing garnet inner-rim compositions (not shown), signifying those just inside of the outermost diffusion-related retrograde inflection also intersect at similar *P–T* conditions to those delimited by modal proportion contours.

3.3. Monte Carlo randomisation procedure

The sensitivity of calculated assemblage field boundaries to this point count-derived bulk composition is subsequently investigated by using a Monte Carlo randomisation procedure that simulates both petrological heterogeneity at the thin-section scale and also uncertainty associated with the calculation of phase proportions (Hirsch, 2012). This procedure involves calculating a randomised proportion for each individual mineral in sample OD68-12, such that this perturbed value lies on a normal (Gaussian) distribution, with μ (the mean) centred on the observed modal proportion, and that two standard deviations (2σ) from μ fall within a set relative threshold of that value. For sample OD68-12, this randomisation technique was implemented twenty times: ten times with a relative threshold of 10% (i.e. $2\sigma = \mu \times 0.1$), and ten times with a relative threshold of 20% (i.e. $2\sigma = \mu \times 0.2$). For example, the original point-counted modal proportion of garnet (11.1%; Table 2) will have 95% (2σ) of its randomly perturbed modal proportions within 1.11% of this value for a 10% relative threshold, and within 2.22% for a 20% relative threshold. Each set of randomised modal proportions were then normalised and used as input parameters for bulk-composition calculation in conjunction with the idealised mineral compositions given in Table 1. All twenty of the perturbed mineral proportions and associated recalculated bulk compositions are given in Table 2.

The extent to which particular assemblage field boundaries shift in *P–T* space in response to this randomisation procedure can be seen in Fig. 6a and b, which show results for a 10% and 20% threshold, respectively. Assemblage field boundaries calculated for the original point count-derived bulk composition (Fig. 5a) are shown as heavy, red lines, whereas those calculated for randomised bulk compositions are given as thin, dark-grey lines enclosed within a light-grey envelope, which delimits the maximum extent of assemblage-field boundary shift in *P–T* space. Alongside examining how the assemblage field boundaries are affected, modal proportion contours for the major minerals biotite (Fig. 6c and f), garnet (Fig. 6d and g), and cordierite (Fig. 6e and h) are shown for both percentage thresholds. Due to the randomisation and normalisation procedure outlined above, each new bulk composition is necessarily associated with an individual set of mineral proportions; thus, the modal proportion contours given in Fig. 6c–h are non-identical to one another. The heavy, dashed contours represent the actual normalised integer-rounded proportion (i.e. *n*%), and light, dashed contours represent a modal proportion of ($n \pm 1$)%, thus providing an indication of the spatial distribution of contours across different assemblage fields. Akin to

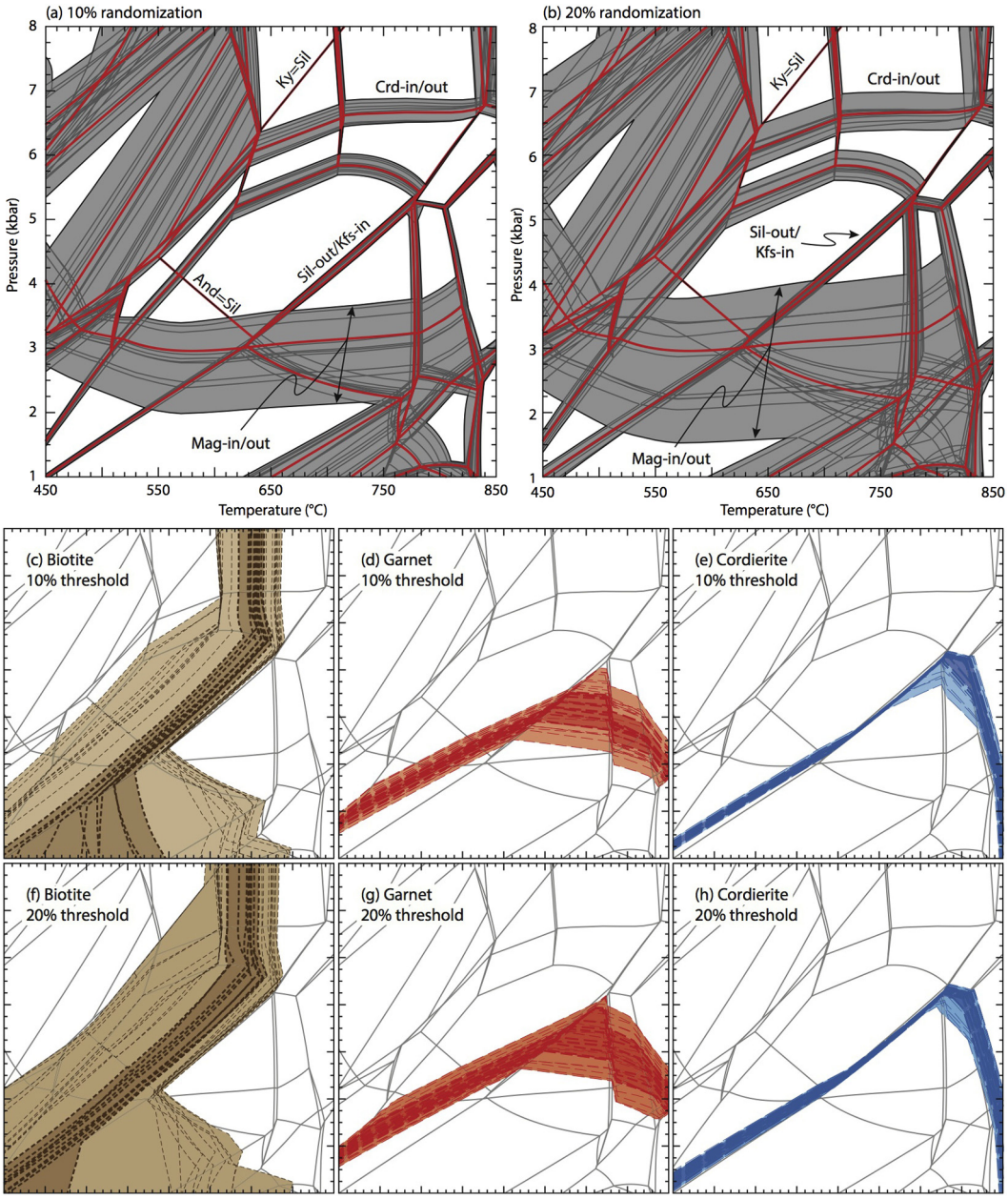

Figure 6. *P–T* pseudosection results following randomisation of the point-count derived sample OD68-12 effective bulk composition via the Monte Carlo method described in the main text. Assemblage fields are shaded according to the number of degrees of freedom, with higher-variance assemblages represented by darker shading. Thresholds for the modal proportion randomisation procedure were set at 10% for part (a) and 20% for part (b). In each case, the calculated assemblage field boundaries for the original (non-randomised) bulk composition (shown in Fig. 5a) are given as heavy, red lines. Assemblage field boundaries for randomised bulk compositions are given as thin, dark-grey lines that are enclosed within a light-grey envelope that highlights the maximum extent of assemblage-field boundary shift in *P–T* space. Parts (c–h) show contours for modal proportion of biotite, garnet, and cordierite for each of the randomised bulk compositions. Heavy, dashed contours represent the target proportion (n%), with light, dashed contours representing an integer modal proportion of ($n \pm 1$)% of the target proportion. Note that the proportion of each mineral represented by the contour set ($n \pm 1$)% varies in accordance with the proportions calculated during the randomisation process and are not identical between diagrams. (c) Biotite, (d) garnet, and (e) cordierite with a randomisation threshold of 10%. (f) Biotite, (g) garnet, and (h) cordierite with a randomisation threshold of 20%. Dark-coloured shaded bands mark the extent of target modal proportion contour shift in *P–T* space, whereas lighter-coloured shaded bands mark the extent of ($n \pm 1$)% modal proportion contour shift in *P–T* space.

the assemblage field boundary line envelopes in Fig. 6a–b, dark-coloured shaded regions delimit the extent of target modal proportion contour shift in *P–T* space, whereas lighter-coloured shaded bands mark the extent of ($n \pm 1$)% modal proportion contour shift in *P–T* space. Calculated pseudosections and associated integer-rounded modal proportion contour sets for all twenty randomised bulk compositions are individually presented in Appendix B.

It is evident from examination of Fig. 6 that certain assemblage field boundaries are significantly more sensitive to bulk-composition perturbation than others. For example, the andalusite-to-sillimanite and sillimanite-to-kyanite polymorphic transitions are bulk composition independent, so they necessarily remain in a fixed position in *P–T* space (though their extent may vary according to expansion or compression of neighbouring fields). The transition between sillimanite-bearing assemblages

and K-feldspar-bearing assemblages that marks the upper-*T* limit of the interpreted peak assemblage field on Fig. 5 occurs across the quinivariant assemblage field Grt–Bt–Sil–Crd–Kfs–Pl–Ilm–Qtz (labelled 'Sil-out/Kfs-in' on Fig. 6a–b). The position of this assemblage field shows only minor variation in *P*–*T* space, as it is closely related to the univariant KFMASH reaction:

$$\mathrm{Bt} + \mathrm{Sil} + \mathrm{Qtz} = \mathrm{Grt} + \mathrm{Crd} + \mathrm{Kfs} + \mathrm{Liq} \quad (1)$$

which provides a fundamental control on low-*P* phase stability in high-grade metapelites. The position of assemblage fields representing higher-variance expressions of this univariant reaction is thus tightly constrained by the KFMASH end-member equilibria, and their variation in *P*–*T* space are weakly controlled by interactions with MnNCKFMASHTO equilibria involving phases containing non-KFMASH components (e.g. TiO_2 in ilmenite, or CaO–Na_2O in plagioclase).

Magnetite was not identified in sample OD68-12, although it has been documented elsewhere in similar garnet- and cordierite-bearing pelitic granofelses from the central Odenwald Crystalline Complex (Okrusch et al., 2000). Calculated phase assemblages for sample OD68-12 (and others; see Fig. 2 of White, R.W. et al., 2014a) indicate that magnetite stability is pressure-sensitive at this low bulk-rock $X_{Fe^{3+}}$, only occurring below ~3 kbar at the temperature range of interest. Although the magnetite-in/out assemblage field boundary lines do not border the interpreted peak assemblage field for the original non-perturbed point-counted bulk-rock composition (Fig. 5), they migrate up- and down-*P* by approximately ±0.5 kbar for assemblages calculated for a 10% relative threshold (Fig. 6a), and by approximately ±1 kbar for assemblages calculated for a 20% relative threshold (Fig. 6b). In each of these cases, its calculated presence serves to restrict the *P*–*T*-extent of the magnetite-absent interpreted peak assemblage field to higher-*P* conditions of ~3.5 kbar and ~4 kbar, respectively. For contact metamorphosed units such as those in the Odenwald Crystalline Complex, it is often desirable to accurately constrain the pressures of metamorphism as a proxy for determining the depth of emplacement of associated magmatic intrusions (e.g. Pownall et al., 2012). Even with a conservative estimate of petrological variation using a 10% relative threshold for modal proportion perturbation, this magnetite-in/out line raises the low-*P* limit of the interpreted peak assemblage field in OD68-12 by ~0.5 kbar (Fig. 6a), and the magnitude of this effect doubles to nearly 1 kbar for a 20% threshold (Fig. 6b). With a representative crustal density of ~2750 kg/m^3 and assuming no tectonic overpressure, 1 kbar is representative of ~3–3.5 km depth within the Earth's crust. Thus, interpretations of the depth of intrusion of a magmatic pluton based on the *P*–*T* extent of a metamorphic phase assemblage field on a pseudosection may vary significantly, potentially influencing tectonic interpretations, as discussed further below.

4. Case study 2: garnet–staurolite–kyanite schist

XRF analysis is commonly used to obtain bulk compositions for metamorphic rocks that are, for example, too fine- or coarse-grained for thin-section scale point counting to be effective. However, where grain sizes are amenable for point counting, it is worthwhile to consider how much an XRF-derived bulk composition differs from that calculated via mineral modal proportions and representative compositions, and whether this affects the ability of phase diagram modelling to accurately reproduce the observed petrographic features in any significant way. This issue is investigated by using a sample of garnet–staurolite–kyanite schist from the Danba Structural Culmination in the Triassic–Jurassic Songpan-Garzê Fold Belt of eastern Tibet (Roger et al., 2010; Weller et al., 2013), from which bulk compositions have been obtained via both techniques.

4.1. Petrography and bulk compositions

Eight bulk-rock compositions were obtained directly from sample W113: one via XRF and seven via point counting of separate thin sections. A ninth 'artificial' bulk composition was calculated indirectly by taking the mean of each of the seven point count-derived compositions, all of which are given in Table 3. Whole-rock major-element data were obtained using XRF analysis of a fused glass bead on a Rigaku RIX-2000 spectrometer at the Department of Geosciences, National Taiwan University, Taiwan, following the procedures outlined in Wang (2004) and Weller et al. (2013). These wt.% oxide data were recalculated into molar proportions of oxides in the MnNCKFMASHTO compositional system, with a reduction made to the measured CaO content based on the presence of apatite. Mineral compositions and modal proportions were obtained using the same techniques outlined above for sample OD68-12, with representative compositional analyses idealised for use in bulk composition calculation (Table 4). Point count-derived bulk compositions produced low bulk-rock $X_{Fe^{3+}}$ values in the range 1–4% (Table 3), which are supported by the presence of ilmenite and absence of magnetite and/or hematite in these mid-crustal amphibolite-facies rocks (cf. Diener and Powell, 2011). Consequently, pseudosection modelling for the XRF-derived bulk composition employed an $X_{Fe^{3+}} = 1\%$. Calculations using a value of 5% (Appendix B) produced negligible differences in calculated phase assemblage fields, with assemblage field boundary shifts of

Table 3
Point-counted mineral proportions calculated from seven thin sections of sample W113 and associated calculated bulk compositions. The W113 XRF-derived whole-rock bulk composition assumes molar $X_{Fe^{3+}} = 1\%$.

Thin section	Normalized point-counted mineral proportions								Anhydrous bulk composition (mol.% oxides)										AKFM co-ordinate			
	St	Ms	Bt	Qtz	Pl	Ilm	Grt	Ky	SiO_2	Al_2O_3	CaO	MgO	FeO	K_2O	Na_2O	TiO_2	MnO	O	A	K	F	M
1	0.4	17.0	26.9	24.3	2.7	0.2	1.4	27.1	61.78	22.46	0.29	5.43	5.62	3.27	0.43	0.57	0.05	0.11	0.61	0.09	0.15	0.15
2	11.0	27.7	24.6	17.7	2.0	0.4	4.4	12.2	57.40	22.39	0.45	5.82	8.64	3.86	0.50	0.69	0.14	0.11	0.55	0.09	0.21	0.14
3	0.0	28.3	33.3	14.8	1.6	0.6	5.0	16.4	56.60	20.81	0.47	7.07	8.72	4.58	0.49	0.98	0.14	0.14	0.51	0.11	0.21	0.17
4	15.4	35.1	25.1	10.8	1.2	0.4	3.4	8.6	53.88	24.38	0.33	6.20	9.24	4.49	0.54	0.71	0.12	0.11	0.55	0.10	0.21	0.14
5	7.0	26.5	30.7	22.2	2.5	0.8	5.8	4.4	59.33	17.21	0.58	6.86	9.87	4.24	0.53	1.09	0.17	0.13	0.45	0.11	0.26	0.18
6	0.0	42.4	29.4	23.6	2.6	0.2	1.8	0.0	64.04	15.06	0.32	6.62	6.83	5.53	0.78	0.64	0.06	0.13	0.44	0.16	0.20	0.19
7	16.8	25.5	24.8	20.7	2.3	0.8	7.2	1.8	57.31	19.45	0.66	6.15	10.97	3.67	0.50	0.98	0.22	0.11	0.48	0.09	0.27	0.15
Average	**7.2**	**28.9**	**27.8**	**19.2**	**2.1**	**0.5**	**4.2**	**10.1**	**58.62**	**20.25**	**0.44**	**6.31**	**8.56**	**4.23**	**0.54**	**0.81**	**0.13**	**0.12**	**0.51**	**0.11**	**0.22**	**0.16**
2 S.D.	14.7	15.9	6.7	10.0	1.1	0.5	4.2	18.9	6.81	6.52	0.28	1.17	3.62	1.47	0.22	0.41	0.12	0.03	0.12	0.05	0.08	0.04
Range	16.8	25.4	8.6	13.5	1.5	0.6	5.8	27.1	10.16	9.32	0.37	1.64	5.34	2.26	0.35	0.52	0.17	0.04	0.17	0.07	0.12	0.05
XRF (original)									**56.15**	**18.86**	**0.19**	**7.76**	**9.27**	**5.40**	**1.23**	**0.97**	**0.12**	**0.05**	**0.46**	**0.13**	**0.22**	**0.19**

Table 4
Representative mineral compositional analyses from sample W113. Idealisation of each individual mineral composition follows the procedures outlined in Appendix 1 of Powell and Holland (2008).

	Electron microprobe-derived composition							"Ideal analysis"						
Mineral	Bt	Grt	Grt	Ilm	Ms	Pl	St	Bt	Grt	Grt	Ilm	Ms	Pl	St
Location	Matrix	Core	Rim	Matrix	Matrix	Matrix	Pblast	Matrix	Core	Rim	Matrix	Matrix	Matrix	Pblast
SiO_2	36.83	36.53	36.54	0.15	45.40	59.97	26.69	-	-	-	-	-	-	-
TiO_2	1.78	0.04	0.06	56.03	0.79	0.02	0.73	-	-	-	-	-	-	-
Al_2O_3	18.98	20.81	20.78	0.18	35.01	24.38	53.21	-	-	-	-	-	-	-
Fe_2O_3	0.00	2.35	2.00	0.00	0.00	0.06	0.00	-	-	-	-	-	-	-
FeO	17.73	28.15	33.13	44.27	1.04	0.00	13.91	-	-	-	-	-	-	-
MnO	0.03	6.04	0.91	0.30	0.00	0.00	0.10	-	-	-	-	-	-	-
MgO	11.01	1.60	3.13	0.19	0.67	0.00	1.88	-	-	-	-	-	-	-
CaO	0.03	5.14	3.19	0.02	0.00	6.23	0.02	-	-	-	-	-	-	-
Na_2O	0.15	0.00	0.00	0.03	1.14	7.57	0.22	-	-	-	-	-	-	-
K_2O	8.96	0.00	0.01	0.05	9.81	0.01	0.00	-	-	-	-	-	-	-
Total	95.50	100.66	99.75	101.22	93.86	98.24	96.76	-	-	-	-	-	-	-
Si	2.76	2.97	2.98	0.00	3.06	2.71	7.52	2.76	3.00	3.00	-	3.06	2.70	7.50
Ti	0.10	0.00	0.00	1.03	0.04	0.00	0.16	0.10	-	-	1.04	-	-	-
Al	1.67	1.98	1.98	0.01	2.78	1.30	17.67	1.67	2.00	2.00	-	2.78	1.30	18.00
Fe^{3+}	0.00	0.11	0.09	0.00	0.00	0.00	0.00	0.06	-	-	0.00	-	-	-
Fe^{2+}	1.11	1.90	2.24	0.95	0.06	0.00	3.28	1.05	1.93	2.27	0.95	0.07	-	3.20
Mn	0.00	0.41	0.06	0.01	0.00	0.00	0.02	0.00	0.42	0.06	0.01	-	-	0.02
Mg	1.23	0.19	0.38	0.01	0.07	0.00	0.79	1.23	0.20	0.38	0.00	0.08	-	0.77
Ca	0.00	0.44	0.28	0.00	0.00	0.31	0.01	-	0.45	0.28	-	-	0.30	-
Na	0.02	0.00	0.00	0.00	0.15	0.68	0.12	-	-	-	-	0.15	0.70	-
K	0.86	0.00	0.00	0.00	0.84	0.00	0.00	1.00	-	-	-	0.85	0.00	-
Sum	7.75	8.00	8.00	2.00	7.00	5.00	29.56	7.87	8.00	8.00	2.00	7.00	5.00	29.50
Oxygen	11	12	12	3	11	8	46	11	12	12	3	11	8	46
X_{Mg}	0.53	0.09	0.14	-	0.53	-	0.19	0.54	0.09	0.14	-	0.53	-	0.19
Alm	-	0.64	0.76	-	-	-	-	-	0.64	0.76	-	-	-	-
Prp	-	0.07	0.13	-	-	-	-	-	0.07	0.13	-	-	-	-
Grs	-	0.15	0.09	-	-	-	-	-	0.15	0.09	-	-	-	-
Sps	-	0.14	0.02	-	-	-	-	-	0.14	0.02	-	-	-	-
X_{An}	-	-	-	-	-	0.31	-	-	-	-	-	-	0.30	-

$X_{Mg} = Fe^{2+}/(Fe^{2+}+Mg)$.
$X_{An} = Ca/(Ca + Na + K)$.

less than 5 °C. Fluid was assumed to be present (H_2O in excess) during prograde and peak metamorphism due to the absence of any previous dehydrating thermal events having affected the region (Huang et al., 2003). A description of the phase diagram modelling setup conditions and a–x relations utilised is given in Appendix A.

Sample W113 contains large centimetre-scale garnet, staurolite, and kyanite porphyroblasts that lie within a strongly foliated matrix defined by biotite, muscovite, plagioclase, quartz, and ilmenite. In contrast to sample OD68-12, calculated modal proportions of minerals in sample W113 show significant variation on the thin section scale, with all being cut in the same orientation perpendicular to the dominant schistosity (Fig. 7). For example, either kyanite or staurolite may be absent from various sections, but may comprise up to 27.1 and 16.8 vol.% of others (Table 3). This variation can be attributed to the coarse-grained, porphyroblastic nature of the sample: a common feature of amphibolite-facies pelites. Though some staurolite porphyroblasts are partially pseudomorphed at their periphery by muscovite (Fig. 7), this is not ubiquitous. Some staurolite grains have mutual straight grain boundaries with kyanite and garnet, suggesting that it was indeed part of the peak equilibrium assemblage, even if the growth of kyanite during metamorphism required its consumption. As such, staurolite is considered as a stable phase, where present. Representative idealised mineral compositions are given in Table 4.

4.2. Pseudosection modelling

A P–T pseudosection constructed for sample W113 using the XRF-derived bulk composition is shown in Fig. 8a, where the peak assemblage Grt–Bt–Pl–St–Ky–Ilm–Ms–Qtz–H_2O is calculated to be stable at ~5.5–7.5 kbar and ~600–620 °C (field number 8). The P–T extent of this field is consistent with the metamorphic field gradient determined for the Danba Structural Culmination by Weller et al. (2013). Although this restricted region of P–T space may appear to provide a well-constrained estimate of the conditions of peak metamorphism, it is apposite to confirm that the calculated phase proportions are similar to the observed values so as to support the reliability of the results (e.g. sample OD68-12). As it is not practical to accurately determine the proportions of minerals in the volume of rock used for XRF analysis, averaged values of each of the seven point-counted thin section proportions were initially assumed to be representative of the sample mineralogy: 7.2% staurolite, 28.9% muscovite, 27.8% biotite, 19.2% quartz, 2.1% plagioclase, 0.5% ilmenite, 4.2% garnet, and 10.1% kyanite (Table 3).

Calculated isomode contours for garnet, biotite, staurolite, and kyanite for this XRF-derived bulk composition are shown in Fig. 8b–e, respectively, where it is clear that there is a poor correlation between the observed and calculated mineral proportions. Contours representing target values (solid lines) for both garnet and biotite lie at higher-P (or lower-T) conditions than the interpreted peak assemblage field (Fig. 8b–c), and neither staurolite nor kyanite show matching target values throughout the P–T range investigated (Fig. 8d–e), with their calculated proportions being underestimated compared to the thin-section average values. Calculated proportions at representative P–T conditions of 6.5 kbar and 615 °C within the centre of the interpreted peak assemblage field are 3.8% staurolite, 41.2% muscovite, 35.2% biotite, 14.1%

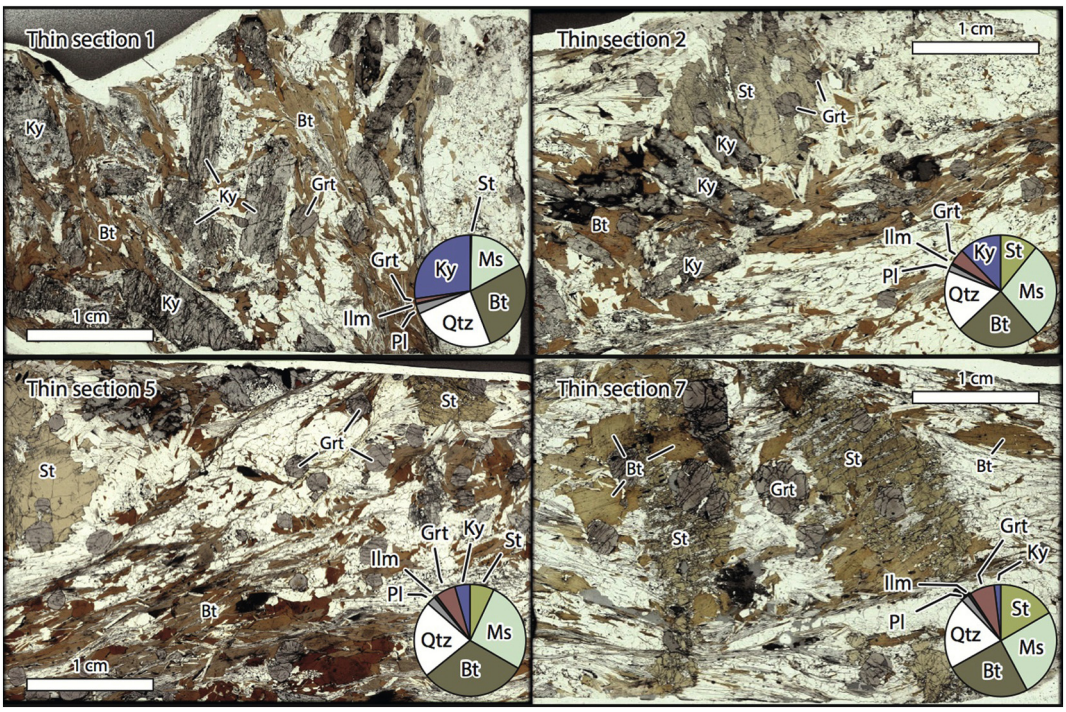

Figure 7. Representative images of thin sections of sample W113 showing variation in observed mineral proportions. Pie chart insets give the relative proportions of minerals garnet, staurolite, kyanite, muscovite, biotite, quartz, plagioclase, and ilmenite. All images are shown at the same scale and the long-axis field of view is approximately 25-mm. Thin-section numbers correlate with those given in Table 3.

quartz, 1.9% plagioclase, 0.8% ilmenite, 1.3% garnet, and 1.3% kyanite, indicating that the discrepancies are largely accommodated by a calculated over-estimation of muscovite and biotite.

Fig. 9 shows four representative *P*–*T* pseudosections calculated for point count-derived bulk compositions obtained from thin sections 1, 2, 5, and 7 (Table 3). Pseudosections for bulk compositions obtained from additional thin sections 3, 4, and 6 are shown in Appendix B. The interpreted peak assemblage field Grt–Bt–Pl–St–Ky–Ilm–Ms–Qtz–H_2O is highlighted in each case and is located at similar *P*–*T* conditions to that for the XRF-derived bulk composition shown in Fig. 8 for all examples excluding thin section 6. Modal proportion contours for garnet, biotite, staurolite, and kyanite are indicated on each pseudosection and are labelled as target integer-rounded values (*n*%), given as solid lines, with sub-

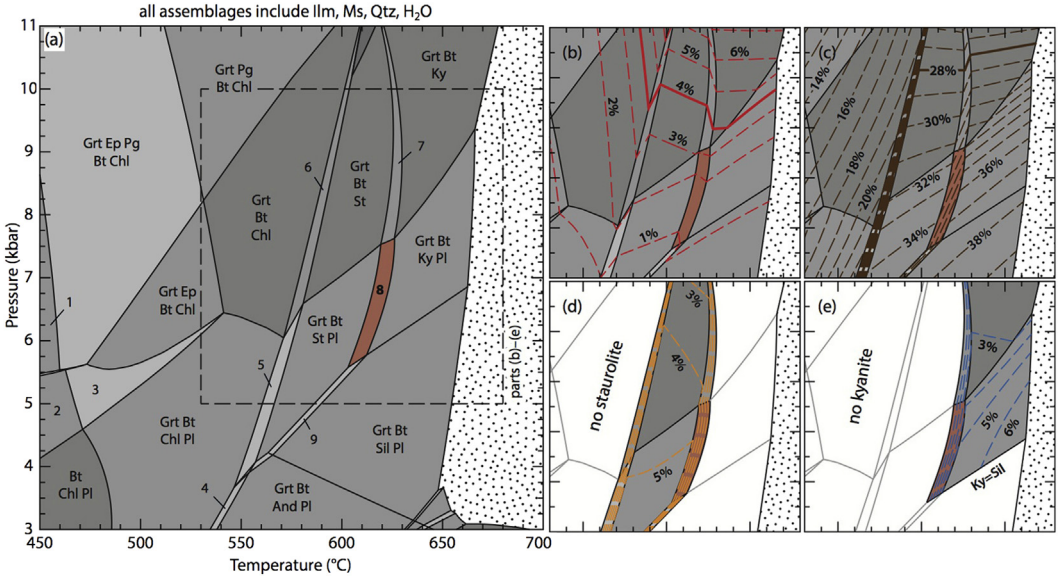

Figure 8. (a) *P*–*T* pseudosection calculated for sample W113 using an XRF-derived bulk composition with $X_{Fe^{3+}} = 1\%$. Assemblage fields are shaded according to the number of degrees of freedom, with lower variance assemblages represented by darker shading. The interpreted peak metamorphic assemblage field is shaded in red and labelled with bold text. Dotted region represents suprasolidus phase assemblages. Numbered fields are as follows: 1 – Bt Ep Chl Pg; 2 – Bt Ep Chl Pl; 3 – Grt Bt Ep Chl Pl; 4 – Grt Bt And Chl Pl; 5 – Grt Bt St Chl Pl; 6 – Grt Bt St Chl; 7 – Grt Bt St Ky; 8 – Grt Bt St Ky Pl; 9 – Grt Bt St Pl Sil. Dashed box represents *P*–*T* limit of parts b–e, which show modal proportion contours for (b) garnet, (c) biotite, (d) staurolite, and (e) kyanite. Heavy, non-dashed modal proportion contours represent observed values (cf. Table 3), where relevant.

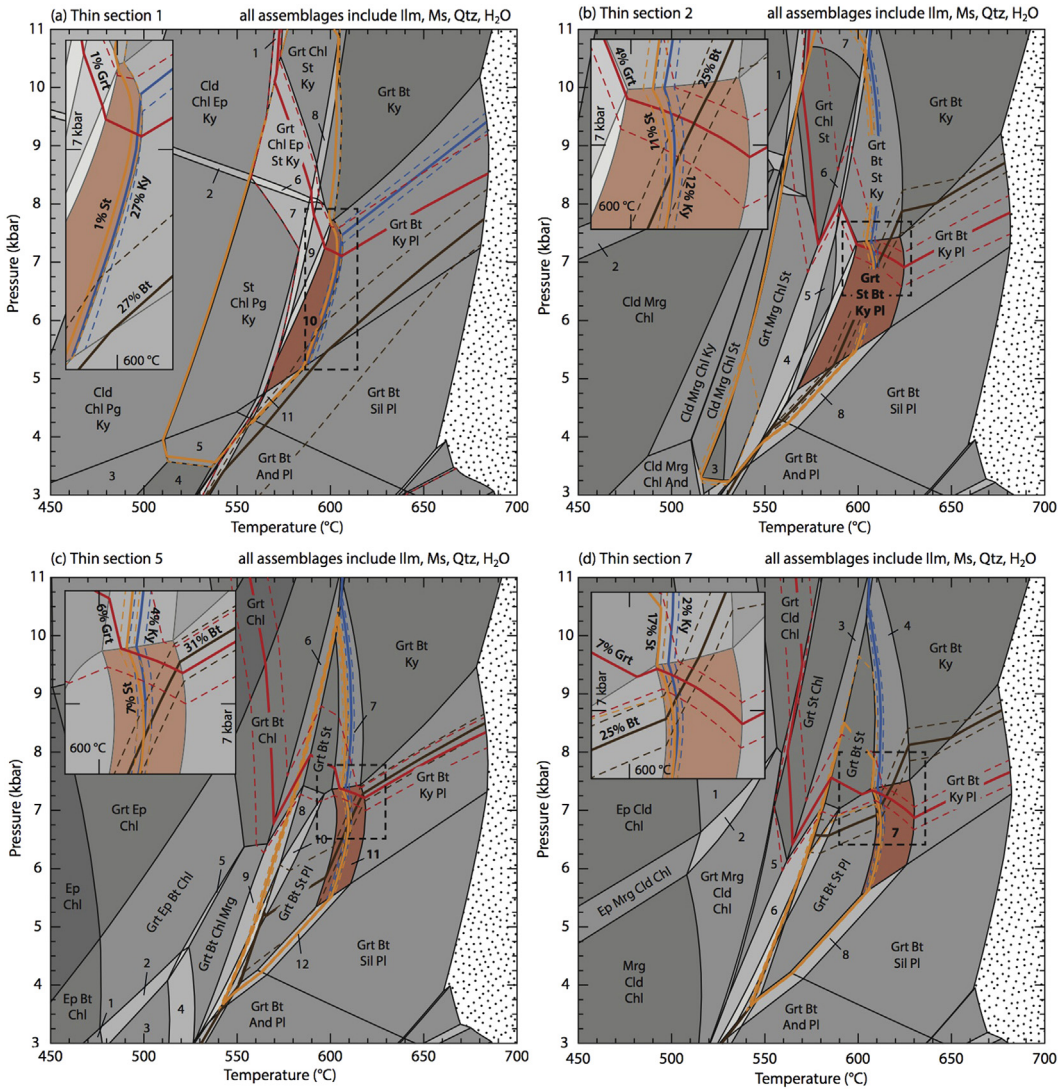

Figure 9. Representative *P–T* pseudosections calculated for bulk compositions derived from different thin sections of sample W113 via point counting. In all cases, dotted regions represent suprasolidus phase assemblages and assemblage fields are shaded according to the number of degrees of freedom, with higher-variance assemblages represented by darker shading. The interpreted peak metamorphic assemblage field is shaded in red and labelled with bold text. Insets show the regions outlined by dashed boxes in enhanced detail. Numbered fields are as follows: (a) 1 – Cld Chl Grt Ep Ky; 2 – Cld Chl Ep Pg Ky; 3 – Cld Chl Pg And; 4 – Chl Pg And; 5 – St Chl Pg And; 6 – Grt Chl Ep St Ky Pg; 7 – Grt St Chl Pg Ky; 8 – Grt Bt Chl St Ky; 9 – Grt St Bt Pg Ky; 10 – Grt Bt Ky St Pl; 11 – Grt Bt Sil St Pl. (b) 1 – Cld Chl Ep; 2 – Cld Mrg Ep Chl; 3 – Mrg Chl St; 4 – Grt Mrg Chl St Bt; 5 – Grt Mrg St Bt; 6 – Grt St Chl Bt; 7 – Grt Chl St Ky; 8 – Grt Bt Sil St Pl. (c) 1 – Ep Bt Chl Pl; 2 – Grt Ep Bt Chl Pl; 3 – Grt Bt Chl Pl; 4 – Grt Bt Chl Pl Mrg; 5 – Grt Ep Bt Chl Mrg; 6 – Grt Bt Chl St; 7 – Grt Bt St Ky; 8 – Grt Bt St Mrg; 9 – Grt Bt Chl Mrg Pl; 10 – Grt Bt St Pl Mrg; 11 – Grt Bt St Ky Pl; 12 – Grt Bt St Sil Pl. (d) 1 – Grt Ep Cld Chl; 2 – Grt Ep Mrg Cld Chl; 3 – Grt St Chl Bt; 4 – Grt Bt St Ky; 5 – Grt St Chl Pl; 6 – Grt St Bt Chl Pl; 7 – Grt Bt Ky St Pl; 8 – Grt Bt Sil St Pl.

parallel dashed lines representing ($n \pm 1$)%. Target values for each phase are not equal between diagrams, instead corresponding to thin section-specific proportions given in Table 3. In each diagram, point-counted target values for garnet, staurolite, and kyanite all converge on a small area of *P–T* space around 7.5 kbar and 610 °C that lies within the interpreted peak assemblage field. For thin sections 2, 5, and 7 (Fig. 9b–d), the target value for biotite also passes close to these regions, although lies ~2 kbar down-*P* for thin section 1 (Fig. 9a). A pseudosection calculated using a bulk composition derived from thin section averaged modal proportions is shown in Fig. 10a and offers a useful comparison to that for the XRF-derived bulk composition (Fig. 8a). Contours for integer-rounded average target modal proportions of garnet (Fig. 10b), biotite (Fig. 10c), staurolite (Fig. 10d), and kyanite (Fig. 10e) converge within the interpreted peak assemblage field at ~7 kbar and 610 °C (Fig. 10a).

These results for XRF- and point count-derived bulk compositions are quite different, despite the interpreted conditions of peak metamorphism determined by the extent of the interpreted equilibrium assemblage in *P–T* space being similar for each (~7.5 kbar and 610 °C). The individual point count-derived bulk compositions provide a very good match between calculated and observed mineral proportions, which is particularly surprising given the large ranges observed between individual thin sections (Table 3). However, a poor correlation exists between the predicted modal proportions of minerals in the peak assemblage field for the XRF-derived bulk composition and those averaged from all seven thin sections, which are thus unlikely to accurately represent the actual 3D-integrated proportions present in sample W113.

The magnitude of variation between each calculated bulk composition can be expressed graphically in AKFM (Al_2O_3–K_2O–FeO–MgO) compositional space (Fig. 11a), with the

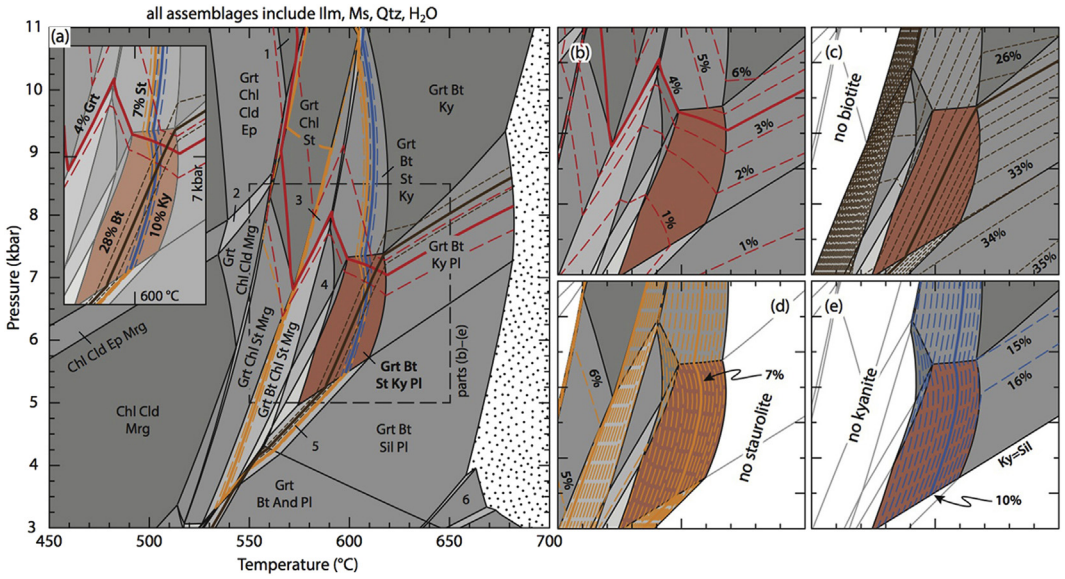

Figure 10. (a) *P–T* pseudosection calculated for a bulk composition derived from average point-counted mineral proportions. Dotted region represents suprasolidus phase assemblages and assemblage fields are shaded according to the number of degrees of freedom, with higher-variance assemblages represented by darker shading. The interpreted peak metamorphic assemblage field is shaded in red and labelled with bold text. Numbered fields are as follows: 1 – Grt Chl Ep; 2 – Grt Chl Cld Ep Mrg; 3 – Grt Bt Chl St; 4 – Grt Bt St Mrg; 5 –Grt Bt St Sil Pl; 6 – Grt Bt Sil Pl Kfs (–Ms). Dashed box represents *P–T* limit of parts b–e, which show modal proportion contours for (b) garnet, (c) biotite, (d) staurolite, and (e) kyanite. Heavy, non-dashed modal proportion contours represent calculated average values (cf. Table 3).

XRF-derived bulk composition located more-or-less within the main cluster of point count-derived bulk compositions, albeit slightly further away from the Al_2O_3 apex. Normalized AKFM co-ordinates for all bulk compositions are given in Table 3. Projection of these data from muscovite onto the AFM plane, with quartz and H_2O in excess (Thompson, 1957), also allows examination of their positions relative to equilibrium phase relationships calculated at estimated peak conditions of 7.5 kbar and 610 °C in the KFMASH compositional system, which is the simplest system in which the key univariant equilibria in metapelites can be represented (Fig. 11b). Despite having a relatively larger wt.% K_2O content than the averaged point-count derived bulk composition (~1.25-times), the XRF-derived bulk composition has very similar AKFM normalized co-ordinates (Fig. 11a) due to K_2O being a proportionally minor component when compared to the absolute amounts of Al_2O_3, FeO, and MgO (Table 3). In fact, the greatest variation in AKFM space occurs in the normalized alumina contents (0.44–0.61; Fig. 11a and Table 3), which have approximately constant FeO:MgO ratios, but show an inverse relationship with K_2O content (Table 3). This is expressed petrologically and on an AFM compatibility diagram by antithetic proportions of mica (matrix) to porphyroblasts (e.g. Figs. 7 and 11b). For example, the most alumina-poor thin section (number 6) contains no staurolite or kyanite – two distinctly Al-rich porphyroblasts – but has a disproportionately high amount of muscovite (~42.4%, compared to the mean value of 28.9%; Table 3).

Such a phenomenon is likely to be an expression of aluminium being one of the most immobile major rock-forming elements

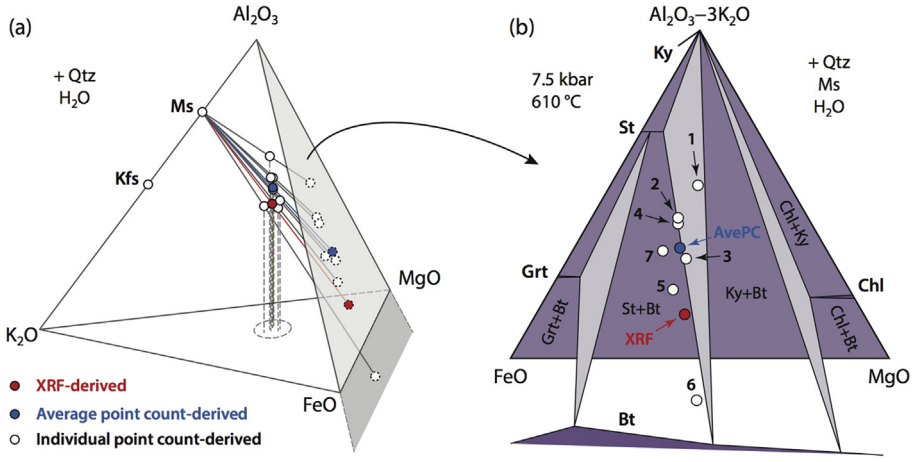

Figure 11. Chemographic projections in the KFMASH compositional system for sample W113. (a) Al_2O_3–K_2O–FeO–MgO (AKFM) tetrahedron with quartz and H_2O in excess showing the position of various bulk compositions calculated for W113 using both methods described in the text. Shaded region on the tetrahedron represents the AFM plane shown in part (b), with the positions of the bulk compositional data derived using a Thompson (1957) projection from muscovite. (b) AFM compatibility diagram calculated at 7.5 kbar and 610 °C with quartz, muscovite, and H_2O in projection. The positions of XRF-derived and point count-derived bulk compositions are marked with circles, with values for individual data points referring to the thin section number given in Table 3.

under metamorphic *P*–*T* conditions (Carmichael, 1969; Rumble, 1982), with its effective length-scale of diffusion being the primary control on the size of the equilibration volume in a metapelite. This, in turn, is an expression of original mineralogical variation across sedimentary layering in the protolith, for example with the relative proportions of quartzofeldspathic material to Al-rich clay minerals (illite, smectite, and/or kaolinite), which control domainal A:K:FM ratios. Whilst it is unlikely that the decimetre-sized volume of W113 used for XRF analysis is larger than the size of the equilibration volume at peak amphibolite-facies *P*–*T* conditions (Fig. 3), it is notably more heterogeneous than sample OD68-12 by virtue of a distinct millimetre-scale spaced foliation and centimetre-scale porphyroblasts (Fig. 7). Thus, point counting is likely to preserve small-scale petrographic features (e.g. Al-rich, porphyroblast-rich domains) that are otherwise averaged out in XRF analysis of a larger sample. Each point count-derived bulk composition appears to be reasonably representative of the sample volume sectioned (Fig. 9), as shown by isomode contours for different phase proportions converging at the same *P*–*T* conditions in the same peak assemblage field, even if any particular thin section is not representative of the sample used for XRF analysis. A much larger number of thin sections of sample W113 than is used here would therefore are required in order to produce a reliable representation of its volume-integrated mineralogy.

5. Discussion and conclusions

Petrological studies involving any form of thermobarometry aim to determine the absolute *P*–*T* conditions of metamorphism for a sample of rock, the relative differences in *P* and/or *T* between multiple samples, or both. These data are typically used to interpret the changing depths in the Earth at which metamorphism and/or deformation took place, thus shedding light on the tectonic settings of formation and the geodynamic processes responsible. Hodges and McKenna (1987) suggested that two of the most significant quantifiable sources of uncertainty in conventional thermobarometry are analytical imprecision and the systematic error associated with experimental calibration techniques, with the latter accounting for 80–90% of the total pressure uncertainty and over 70% of the total temperature uncertainty for any particular calibration. When a single pair of equilibria is used for comparative purposes, the systematic experimental-related errors cancel, leaving only random uncertainty associated with analytical imprecision as a contributing factor. Nonetheless, these remaining errors are cited to be at least ±1 kbar and ±50 °C at the 2σ level (Hodges and McKenna, 1987; Kohn and Spear, 1991; Powell and Holland, 2008), meaning that discrimination between multiple datasets using the same geobarometer is only statistically valid for a difference of at least ~6–7 km of crustal thickness. Furthermore, this uncertainty should be considered as a minimum given the possibility of disequilibrium within the considered mineral assemblage.

The *P*–*T* extent of a field on a pseudosection corresponding to the interpreted equilibrium peak assemblage can often be smaller than these ±1 kbar and ±50 °C values associated with conventional thermobarometry (e.g. Fig. 9), making phase equilibria modelling a more attractive (although labour-intensive) technique for detailed investigation of the tectonothermal evolution of a metamorphic rock. Even when this is not the case, refinement of *P*–*T* conditions in large fields can be achieved by contouring for mineral proportions and/or compositions, as shown for sample OD68-12 (Fig. 5). Many studies alternatively use mineral compositions for the same delimiting purposes, in particular isopleths for garnet end-member proportions (Evans, 2004), given that they represent a single stochiometrically constrained equilibrium as opposed to an interpreted equilibrium based on the compositions of multiple touching grains.

The two case study examples described above show that minor variations in the bulk composition used for pseudosection modelling could upset this idealised workflow. Although pseudosection analysis of sample OD68-12, a well-equilibrated and texturally homogenous garnet–cordierite–granofels, proved successful in terms of matching observed and calculated minerals at *P*–*T* conditions of peak metamorphism, only minor variation in the modal proportions of each phase was sufficient to cause important assemblage field boundaries to shift in *P*–*T* space. A relative perturbation of 10% on observed mineral proportions caused the pressure-sensitive magnetite-in/out field boundary to migrate up/down-*P* by ~0.5 kbar, and a larger perturbation of 20% effectively doubled this transposition to approximately ±1 kbar (Fig. 6). Importantly, however, assemblage fields representing higher-variance equivalents of KFMASH univariant reactions are significantly less sensitive to bulk composition variation and therefore provide more reliable constraints on the *P*–*T* conditions of metamorphism. Evans and Bickle (2005) reported a similar result whereby propagated errors on thermodynamic dataset end-members for accessory/minor minerals could lead to uncertainties on calculated modal proportions on a pseudosection of up to 30%. Although the 10% (or even 20%) threshold for mineral modal proportion variation considered here might appear gratuitous when compared to the accuracy of point-count methods available (e.g. Hirsch, 2012), it is easily justifiable when considered in the context of the "unseen" third dimension associated with thin section preparation procedures.

For XRF-derived bulk compositions, mineral proportions and compositions used to compare calculated phase equilibria with natural parageneses must be obtained via electron microprobe analysis of a 2D thin section; however, it is unlikely that the observed proportions in a profile match those present in a 3D volume, even if the thin section is cut from the same block used for XRF analysis, as is common practice. This point is demonstrated well for amphibolite-facies metapelite sample W113, where a poor correlation was observed between modal proportions of minerals predicted to be present within the interpreted peak assemblage field on an XRF-derived pseudosection, compared to average values determined from several thin sections. Given that correlations between observed and calculated modal proportions were notably better for point count-derived bulk compositions, it is clear that the mineral proportions obtained via averaging multiple thin sections do not effectively represent those present in the rock as a whole, unless dealing with an extremely homogenous or fine-grained lithology. Despite this, the point count-derived bulk compositions appear to be representative of the much smaller centimetre-scale sample volume from which they were cut, even if they are not representative of the larger decimetre-scale block used for XRF analysis, and so have value in the pseudosection modelling process. The main differences between both techniques reflect varying proportions of matrix relative to porphyroblasts, which we relate to protolith sedimentological variation, with original clay-rich horizons locally forming porphyroblast-rich layers in the metamorphic environment due to Al-immobility.

5.1. Complexities related to an evolving equilibration volume

The case study examples discussed above assume that all MnNCKFMASHTO-compatible mineral constituents are part of each respective effective bulk composition; however, minor components such as MnO that preferentially enter garnet cores may become unable to chemically communicate with the matrix during its growth until temperatures allow diffusional equilibration on length

scales exceeding that of the porphyroblast radius (Spear, 1988; White, R.W. et al., 2014b). Although the actual (Fig. 3a) and model-ready (Fig. 3b) bulk compositions do not change during element fractionation, the effective bulk composition will (Fig. 3c). As such, the amount of rock representative of an equilibration volume that can be replicated via pseudosection modelling dynamically changes in space and time, owing to the distinctly different mobilities of different elemental species under varying metamorphic conditions (White et al., 2008). Open-system processes such as the percolation of melts, fluids, or brines may additionally drive reactions via bulk-composition changes (e.g. alkali metasomatism) on a local or regional scale, promoting mineralogical change that cannot be accounted for solely by changing *P*–*T* conditions in a closed-system environment (e.g., White, A.J.R. et al., 2014).

Equilibration volumes in a rock are likely to be largest at high temperatures and will contract with cooling such that minerals that were once in equilibrium become unable to chemically communicate during retrograde metamorphism. The formation of different equilibration volumes comprised of multiple grains of different minerals produces domains with different effective bulk compositions than that of the entire rock, and thus different equilibrium phase assemblages can form in each. More importantly, unless the mineral proportions in a particular domain exactly match those of the whole rock, a pseudosection used to investigate a rock's petrological evolution during prograde and/or peak metamorphism is unsuitable for investigating mineralogical change that occurs in chemically isolated domains during retrogression. Conventional thermobarometry can be used estimate the conditions of mineralogical change in this situation (e.g. Palin et al., 2013a), where suitable pressure- and/or temperature-sensitive minerals have recrystallised. However, a comprehensive assessment of the time-evolution of an equilibration volume must incorporate chemical potential fields that consider the effects of cooling through a temperature range over which the diffusion of chemical components for any given length scale becomes sequentially ineffective. This issue will be explored in a future publication.

5.2. Implications for tectonic interpretations and concluding remarks

The identification of relative or absolute changes in *P*–*T* conditions during metamorphism is a fundamental step in elucidating the geodynamic processes that have affected a geological terrane. While some workers have performed pseudosection analysis using bulk compositions averaged from multiple petrologically similar samples (e.g. Chen et al., 2008; Reche and Martinez, 2008; Zhang et al., 2012), our case study example for sample OD68-12 warns that important limiting assemblage field boundaries may migrate in *P*–*T* space by unknown (but potentially significant) amounts. Even small differences in bulk compositions identified in the same sample (e.g. W113) lead to distinct differences in pseudosection topologies and associated mineral compositions and modal proportions (Figs. 7–10). In a recent study, Pattison and DeBuhr (2015) used pseudosection modelling of metapelites from around the Bugaboo Batholith, British Columbia, to constrain different pressures of metamorphism on either side of the contact aureole. Given the similar present-day levels of exposure, these data were taken to infer post-intrusion tilting in the region; however, the absolute difference in pressure across the aureole was reported to be ~0.3 kbar, which is significantly smaller than the minimum resolvable limit even for comparative studies using conventional thermobarometry (Hodges and McKenna, 1987; Kohn and Spear, 1991; Powell and Holland, 2008). Although such small fields may be identifiable on a pseudosection, it is important to recognise that the sources of error concerning bulk-composition determination, as shown in this study, can be larger still. It is perhaps an inconvenient truth that such small differences in pressure or temperature cannot be resolved with statistical certainty by using currently available techniques; whether conventional thermobarometry or phase equilibria modelling.

As such, although phase diagrams constructed with currently available *a*–*x* relations and thermodynamic datasets satisfactorily reproduce broad patterns of field observations, literal interpretation of calculated pseudosections is not recommended, not least due to frequent updates to internally consistent thermodynamic datasets and *a*–*x* relations that can affect the stabilities of even simple calculated mineral assemblages (cf. Green et al., 2013; White, R.W. et al., 2014a). In particular, the range of uncertainties associated with these modelling procedures calls into question the veracity of studies that employ such techniques to investigate non-equilibrium behaviour of natural rock systems, such as overstepping of reactions requiring nucleation of a new phase. Though these processes have been demonstrated to be important in certain natural cases (Waters and Lovegrove, 2002), the magnitude of transposition of assemblage-field boundary positions in *P*–*T* space caused simply by geological error as shown here casts doubt on the ability of pseudosections to provide meaningful data in these scenarios. Nonetheless, a phase equilibria modelling approach is highly valuable for deducing general *P*–*T* trends, as long as the absolute *P*–*T* conditions are not over-interpreted. Careful consideration of the size of the equilibration volume, the constituents that comprise the bulk composition used for modelling, and the best technique to employ for its determination based on rock type and petrographic character, offer the best chance to produce trustworthy data from pseudosection analysis.

Acknowledgements

RMP acknowledges a NERC postgraduate grant (reference number NE/H524781/1) for funding analytical work performed at the University of Oxford, UK. The Mineralogical Society of Great Britain and Metamorphic Studies Group of the Geological Society of London, UK, are thanked for a travel grant that allowed attendance of fieldtrip to the Odenwald Crystalline Complex following the 1st European Mineralogical Conference (Frankfurt, Germany) in 2012. M. Okrusch is thanked for supplying sample OD68-12 and for allowing its use in this work. An informal review by R. Berman (Geological Survey of Canada; GSC) helped to improve an early version of the manuscript. We thank anonymous and Catherine Mottram (UCSB) for two highly detailed, thorough, and insightful sets of formal review comments on our manuscript. Co-Editor in Chief Prof. M. Santosh is warmly thanked for extremely efficient editorial handling and his initial invitation to write this contribution for Geoscience Frontiers. This manuscript is GSC contribution number 2015273.

Appendix A. Supplementary data

Supplementary data related to this article can be found at http://dx.doi.org/10.1016/j.gsf.2015.08.005

References

Angiboust, S., Langdon, R., Agard, P., Waters, D.J., Chopin, C., 2011. Eclogitization of the Monviso ophiolite (W. Alps) and implications on subduction dynamics. Journal of Metamorphic Geology 30, 37–61. http://dx.doi.org/10.1111/j.1525-1314.2011.00951.x.

Argles, T.W., Prince, C.I., Foster, G.L., Vance, D., 1999. New garnets for old? Cautionary tales from young mountain belts. Earth and Planetary Science Letters 172, 301–309. http://dx.doi.org/10.1016/S0012-821X(99)00209-5.

Baxter, E.F., Caddick, M.J., Ague, J.J., 2013. Garnet: common mineral, uncommonly useful. Elements 9, 415–419. http://dx.doi.org/10.2113/gselements.9.6.415.

Berman, R.G., 1988. Internally-consistent thermodynamic data for stoichiometric minerals in the system Na_2O–K_2O–CaO–MgO–FeO–Fe_2O_3–Al_2O_3–SiO_2–TiO_2–H_2O–CO_2. Journal of Petrology 29, 445–522. http://dx.doi.org/10.1093/petrology/29.2.445.

Büttner, S.H., 2012. Rock maker: an MS Excel™ spreadsheet for the calculation of rock compositions from proportional whole rock analyses, mineral compositions, and modal abundance. Mineralogy and Petrology 104, 129–135. http://dx.doi.org/10.1007/s00710-011-0181-7.

Caddick, M.J., Bickle, M.J., Harris, N.B.W., Holland, T.J.B., Horstwood, M.S.A., Parrish, R.R., Ahmad, T., 2007. Burial and exhumation history of a Lesser Himalayan schist: recording the formation of an inverted metamorphic sequence in NW India. Earth and Planetary Science Letters 3–4, 375–390. http://dx.doi.org/10.1016/j.epsl.2007.09.011.

Caddick, M.J., Konopásek, J., Thompson, A.B., 2010. Preservation of garnet growth zoning and the duration of prograde metamorphism. Journal of Petrology 51, 2327–2347. http://dx.doi.org/10.1093/petrology/egq059.

Carmichael, D.M., 1969. On the mechanism of prograde metamorphic reactions in quartz-bearing pelitic rocks. Contributions to Mineralogy and Petrology 20, 244–267. http://dx.doi.org/10.1007/BF00377479.

Carson, C.J., Powell, R., Clarke, G.L., 1999. Calculated mineral equilibria for eclogites in CaO–Na_2O–FeO–MgO–Al_2O_3–SiO_2–H_2O: application to the Pouébo Terrane, Pam Peninsula, New Caledonia. Journal of Metamorphic Geology 17, 9–24. http://dx.doi.org/10.1046/j.1525-1314.1999.00177.x.

Chen, Y., Ye, K., Liu, J.B., Sun, M., 2008. Quantitative *P*–*T*–*X* constraints on orthopyroxene-bearing high-pressure granulites in felsic–metapelitic rocks: evidence from the Huangtuling granulite, Dabieshan Orogen. Journal of Metamorphic Geology 26, 1–15. http://dx.doi.org/10.1111/j.1525-1314.2007.00742.x.

Chinner, G.A., 1960. Pelitic gneisses with varying ferrous/ferric ratios from Glen Clova, Angus, Scotland. Journal of Petrology 1, 178–217. http://dx.doi.org/10.1093/petrology/1.1.178.

Connolly, J.A.D., 1990. Multivariable phase-diagrams – an algorithm based on generalized thermodynamics. American Journal of Science 290, 666–718. http://dx.doi.org/10.2475/ajs.290.6.666.

De Capitani, C., 1994. Gleichgewichts-Phasendiagramme: Theorie und Software. Beihefte zum European Journal of Mineralogy, 72. Jahrestagung der Deutschen Mineralogischen Gesellschaft 6, 48.

Diener, J.F.A., Powell, R., 2011. Revised activity–composition modes for clinopyroxene and amphibole. Journal of Metamorphic Geology 30, 131–142. http://dx.doi.org/10.1111/j.1525-1314.2011.00959.x.

Diener, J.F.A., Powell, R., 2012. Revised activity–composition models for clinopyroxene and amphibole. Journal of Metamorphic Geology 30, 131–142.

Diener, J.F.A., Powell, R., White, R.W., Holland, T.J.B., 2007. A new thermodynamic model for clino- and orthoamphiboles in the system Na_2O–CaO–FeO–MgO–Al_2O_3–SiO_2–H_2O–O. Journal of Metamorphic Geology 25, 631–656. http://dx.doi.org/10.1111/j.1525-1314.2007.00720.x.

Dyck, B., Reno, B.L., Kokfelt, T.F., 2015. The Majorqaq belt: a record of Neoarchaean orogenesis during final assembly of the North Atlantic Craton, southern West Greenland. Lithos 220–223, 253–271. http://dx.doi.org/10.1016/j.lithos.2015.01.024.

Evans, T.P., 2004. A method for calculating effective bulk composition modification due to crystal fractionation in garnet-bearing schist: implications for isopleth thermobarometry. Journal of Metamorphic Geology 22, 547–557. http://dx.doi.org/10.1111/j.1525-1314.2004.00532.x.

Evans, K.A., Bickle, M.J., 2005. An investigation of the relationship between bulk composition, inferred reaction progress, and fluid-flow parameters for layered micaceous carbonates from Maine, USA. Journal of Metamorphic Geology 23, 181–197. http://dx.doi.org/10.1111/j.1525-1314.2005.00571.x.

Green, E.C.R., White, R.W., Powell, R., 2013. Exploring Uncertainties in Phase Diagram Calculations via a Monte Carlo Method. Abstract for pre-Goldschmidt 2013 workshop "Applying phase equilibria modelling to rocks", Florence, Italy.

Guiraud, M., Powell, R., Rebay, G., 2001. H_2O in metamorphism and unexpected behaviour in the preservation of metamorphic mineral assemblages. Journal of Metamorphic Geology 19, 445–454. http://dx.doi.org/10.1046/j.0263-4929.2001.00320.x.

Helgeson, H.C., Delaney, J.M., Nesbitt, H.W., Bird, D.K., 1978. Summary and critique of the thermodynamic properties of rock-forming minerals. American Journal of Science 278A, 1–229.

Hirsch, D.M., 2012. ModeMaker and ModeQuiz: tools for enhancing student learning estimation skills of rock-component abundance. Journal of Geoscience Education 60, 277–287. http://dx.doi.org/10.5408/11-254.1.

Hodges, K.V., McKenna, L.W., 1987. Realistic propagation of uncertainties in geologic thermobarometry. American Mineralogist 72, 671–680.

Holland, T.J.B., Powell, R., 1998. An internally-consistent thermodynamic dataset for phases of petrological interest. Journal of Metamorphic Geology 16, 309–344. http://dx.doi.org/10.1111/j.1525-1314.1998.00140.x.

Holland, T.J.B., Powell, R., 2011. An improved and extended internally consistent thermodynamic dataset for phases of petrological interest, involving a new equation of state for solids. Journal of Metamorphic Geology 29, 333–383. http://dx.doi.org/10.1111/j.1525-1314.2010.00923.x.

Hoschek, G., 2004. Comparison of calculated *P*–*T* pseudosections for a kyanite eclogite from the Tauern Window, Eastern Alps, Austria. European Journal of Mineralogy 16, 59–72. http://dx.doi.org/10.1127/0935-1221/2004/0016-0059.

Huang, M., Buick, I.S., Hou, L.W., 2003. Tectonometamorphic evolution of the Eastern Tibet Plateau: evidence from the Central Songpan-Garzê Orogenic Belt, Western China. Journal of Petrology 44, 255–278. http://dx.doi.org/10.1093/petrology/44.2.255.

Indares, A., White, R.W., Powell, R., 2008. Phase equilibria modelling of kyanite-bearing anatectic paragneisses from the central Grenville Province. Journal of Metamorphic Geology 26, 815–836. http://dx.doi.org/10.1111/j.1525-1314.2008.00788.x.

Kohn, M.J., Spear, F.S., 1991. Error propagation for barometers: 2. Application to rocks. American Mineralogist 76, 138–147.

Kohn, M.J., Spear, F.S., 2000. Retrograde net transfer reaction insurance for pressure–temperature estimates. Geology 28, 1127–1130. http://dx.doi.org/10.1130/0091-7613(2000)28<1127:RNTRIF>2.0.CO;2.

Khorzhinskii, D.S., 1959. Physicochemical Basis of the Analysis of the Paragenesis of Minerals. Consultants Bureau, New York, p. 142.

Kretz, R., 1983. Symbols for rock-forming minerals. American Mineralogist 68, 277–279.

Krohe, A., 1991. Emplacement of synkinematic plutons in the Variscan Odenwald (Germany) controlled by transtensional tectonics. Geologische Rundschau 80, 391–409. http://dx.doi.org/10.1007/BF01829373.

Matte, P., 2001. The Variscan collage and orogeny (480–290 Ma) and the tectonic definition of the Armorica microplate: a review. Terra Nova 13, 122–128. http://dx.doi.org/10.1046/j.1365-3121.2001.00327.x.

Marmo, B., Clarke, G.L., Powell, R., 2002. Fractionation of bulk rock composition due to porphyroblast growth: effects on eclogite-facies mineral equilibria, Pam Peninsula, New Caledonia. Journal of Metamorphic Geology 20, 151–165. http://dx.doi.org/10.1046/j.0263-4929.2001.00346.x.

Mottram, C.M., Warren, C.J., Regis, D., Roberts, N.M.W., Harris, N.B.W., Argles, T.W., Parrish, R.R., 2014. Developing an inverted Barrovian sequence; insights from monazite petrochronology. Earth and Planetary Science Letters 403, 418–431. http://dx.doi.org/10.1016/j.epsl.2014.07.006.

Okrusch, M., 1995. Mid-German crystalline high: IV.E. Metamorphic evolution. In: Dallmeyer, R.D., et al. (Eds.), Pre-Permian Geology of Central and Eastern Europe. Springer-Verlag, Heidelberg, pp. 201–213.

Okrusch, M., Schubert, W., Stähle, V., 2000. The Odenwald, Germany: Variscan metamorphic evolution and igneous events. European Journal of Mineralogy, Beihefte 12, 45–89.

Palin, R.M., Searle, M.P., Waters, D.J., Horstwood, M.S.A., Parrish, R.R., 2012. Combined thermobarometry and geochronology of peraluminous metapelites from the Karakoram metamorphic complex, North Pakistan; new insight into the tectonothermal evolution of the Baltoro and Hunza regions. Journal of Metamorphic Geology 30, 793–820. http://dx.doi.org/10.1111/j.1525-1314.2012.00999.x.

Palin, R.M., Searle, M.P., Waters, D.J., Parrish, R.R., Roberts, N.M.W., Horstwood, M.S.A., Yeh, M.W., Chung, S.L., Anh, T.T., 2013a. A geochronological and petrological study of anatectic paragneiss and associated granite dykes from the Day Nui Con Voi metamorphic core complex, North Vietnam; constraints upon the timing of metamorphism within the Red River shear zone. Journal of Metamorphic Geology 31, 359–387. http://dx.doi.org/10.1111/jmg.12025.

Palin, R.M., Searle, M.P., Morley, C.K., Charusiri, P., Horstwood, M.S.A., Roberts, N.M.W., 2013b. Timing of metamorphism of the Lansang gneiss and implications for motion along the Mae Ping (Wang Chao) strike-slip fault, Thailand. Journal of Asian Earth Sciences 76, 120–136. http://dx.doi.org/10.1016/j.jseaes.2013.01.021.

Palin, R.M., St-Onge, M.R., Waters, D.J., Searle, M.P., Dyck, B., 2014a. Phase equilibria modelling of retrograde amphibole and clinozoisite in mafic eclogite from the Tso Morari massif, northwest India: constraining the *P*–*T*–*M*(H_2O) conditions of exhumation. Journal of Metamorphic Geology 32, 675–693. http://dx.doi.org/10.1111/jmg.12085.

Palin, R.M., Searle, M.P., St-Onge, M.R., Waters, D.J., Roberts, N.M.W., Horstwood, M.S.A., Parrish, R.R., Weller, O.M., Chen, S., Yang, J., 2014b. Monazite geochronology and petrology of kyanite- and sillimanite-grade migmatites from the northwestern flank of the eastern Himalayan syntaxis. Gondwana Research 26, 323–347. http://dx.doi.org/10.1016/j.gr.2013.06.022.

Pattison, D.R.M., DeBuhr, C.L., 2015. Petrology of metapelites in the Bugaboo aureole, British Columbia, Canada. Journal of Metamorphic Geology 33, 437–462. http://dx.doi.org/10.1111/jmg.12128.

Pearce, M.A., White, A.J.R., Gazley, M.F., 2015. TCInvestigator: automated calculation of mineral mode and composition contours for THERMOCALC pseudosections. Journal of Metamorphic Geology 33, 413–425. http://dx.doi.org/10.1111/jmg.12126.

Phillips, G., Hand, M., Offler, R., 2008. *P*–*T*–*t* deformation framework of an accretionary prism, southern New England Orogen, Eastern Australia: Implications for blueschist exhumation and metamorphic switching. Tectonics 27, TC6017. http://dx.doi.org/10.1029/2008TC002323.

Pitra, P., De Waal, S.A., 2001. High-temperature, low-pressure metamorphism and development of prograde symplectites, Marble Hall Fragment, Bushveld Complex (South Africa). Journal of Metamorphic Geology 19, 311–325. http://dx.doi.org/10.1046/j.1525-1314.2001.00313.x.

Plumhoff, A.M., Palin, R.M., White, R.W., Johnson, T.E., Spear, F., 2015. Phase Equilibria Modelling of Barrovian Metamorphism from the Type Locality, Scotland. Abstract for AGU Northeastern Section – 50th Annual Meeting (23–25 March 2015).

Powell, R., 1978. Equilibrium Thermodynamics in Petrology. Harper and Row, London, p. 284.

Powell, R., Holland, T.J.B., 1994. Optimal geothermometry and geobarometry. American Mineralogist 79, 120–133.

Powell, R., Holland, T.J.B., 1988. An internally consistent dataset with uncertainties and correlations: 3. Application to geobarometry, worked examples, and a computer program. Journal of Metamorphic Geology 6, 173–204. http://dx.doi.org/10.1111/j.1525-1314.1988.tb00415.x.

Powell, R., Holland, T.J.B., 2008. On thermobarometry. Journal of Metamorphic Geology 26, 155–179.

Powell, R., Holland, T.J.B., Worley, B., 1998. Calculating phase diagrams involving solid solutions via non-linear equations, with examples using THERMOCALC. Journal of Metamorphic Geology 16, 577–588. http://dx.doi.org/10.1111/j.1525-1314.1998.00157.x.

Powell, R., Guiraud, M., White, R.W., 2005. Truth and beauty in metamorphic phase-equilibria: conjugate variables and phase diagrams. The Canadian Mineralogist 43, 21–33.

Pownall, J.M., Waters, D.J., Searle, M.P., Shail, R.K., Robb, L.J., 2012. Shallow laccolithic emplacement of the land's end and tregonning granites, Cornwall, UK: evidence from aureole field relations and *P–T* modelling of cordierite–anthophyllite hornfels. Geosphere 8, 1467–1504. http://dx.doi.org/10.1130/GES00802.1.

Pownall, J.M., Hall, R., Armstrong, R.A., Forster, M.A., 2014. Earth's youngest known ultrahigh-temperature granulites discovered on Seram, eastern Indonesia. Geology 42, 279–282. http://dx.doi.org/10.1130/G35230.1.

Reche, J., Martinez, F.J., 2008. Exhumation of H*T*–L*P* Variscan metapelites from interlayered cordierite–orthoamphibole assemblages (MnNCFMASH System) Catalan Coastal ranges, NE Iberia. Comptes Rendus Geoscience 340, 288–297. http://dx.doi.org/10.1016/j.crte.2007.12.008.

Robinson, P., 1991. The eye of the petrographer, the mind of the petrologist. American Mineralogist 76, 1781–1810.

Roduit, N., 2010. JMicroVision: un logiciel d'analyse d'images pétrographiques innovant: Étude sur différentes méthodes de quantification et de caractérisation des roches. Éditions universitaires Européennes, p. 136.

Roger, F., Jolivet, M., Malavieille, J., 2010. The tectonic evolution of the Songpan-Garzê (North Tibet) and adjacent areas from proterozoic to present: a synthesis. Journal of Asian Earth Sciences 39, 254–269. http://dx.doi.org/10.1016/j.jseaes.2010.03.008.

Rumble, D., 1982. The role of perfectly mobile components in metamorphism. Annual Review of Earth and Planetary Sciences 109, 221–233. http://dx.doi.org/10.1146/annurev.ea.10.050182.001253.

Spear, F.S., 1988. Metamorphic fractional crystallization and internal metasomatism by diffusional homogenization of zoned garnets. Contributions to Mineralogy and Petrology 99, 507–517. http://dx.doi.org/10.1007/BF00371941.

Stein, E., Dietl, C., 2001. Hornblende thermobarometry of granitoids from the Central Odenwald (Germany) and their implications for the geotectonic development of the Odenwald. Mineralogy and Petrology 72, 185–207. http://dx.doi.org/10.1007/s007100170033.

St-Onge, M.R., Rayner, N., Palin, R.M., Searle, M.P., Waters, D.J., 2013. Integrated pressure–temperature–time constraints for the Tso Morari dome (NW India): Implications for the burial and exhumation path of UHP units in the western Himalaya. Journal of Metamorphic Geology 31, 469–504. http://dx.doi.org/10.1111/jmg.12030.

Štípská, P., Powell, R., 2005. Constraining the *P–T* path of a MORB-type eclogite using pseudosections, garnet zoning, and garnet–clinopyroxene thermometry: an example from the Bohemian Massif. Journal of Metamorphic Geology 23, 725–743. http://dx.doi.org/10.1111/j.1525-1314.2005.00607.x.

Stüwe, K., 1997. Effective bulk composition changes due to cooling: a model predicting complexities in retrograde reaction textures. Contributions to Mineralogy and Petrology 129, 43–52. http://dx.doi.org/10.1007/s004100050322.

Thompson, J.B., 1957. The graphical analysis of mineral assemblages in pelitic schists. American Mineralogist 42, 842–858.

Thompson, J.B., 1959. Local equilibrium in metasomatic processes. In: Abelson, P.H. (Ed.), Researches in Geochemistry. Wiley, New York, pp. 427–457.

Vance, D., Mahar, E., 1998. Pressure-temperature paths from *P–T* pseudosections and zoned garnets: potential, limitations, and examples from the Zanskar Himalaya, NW India. Contributions to Mineralogy and Petrology 132, 225–245. http://dx.doi.org/10.1007/s004100050419.

Wang, K.L., 2004. Geochemical constraints for the genesis of post-collisional magmatism and the geodynamic evolution of the Northern Taiwan region. Journal of Petrology 45, 975–1011. http://dx.doi.org/10.1093/petrology/egh001.

Waters, D.J., Charnley, N.R., 2002. Local equilibrium in polymetamorphic gneiss and the titanium substitution in biotite. American Mineralogist 87, 383–396.

Waters, D.J., Lovegrove, D.P., 2002. Assessing the extent of disequilibrium and overstepping of prograde metamorphic reactions in metapelites from the Bushveld Complex aureole, South Africa. Journal of Metamorphic Geology 20, 135–149. http://dx.doi.org/10.1046/j.0263-4929.2001.00350.x.

Weller, O.M., St-Onge, M.R., Searle, M.P., Rayner, N., Waters, D.J., Chung, S.L., Palin, R.M., Lee, Y.H., Xu, X.W., 2013. Quantifying Barrovian metamorphism in the Danba Structural culmination of eastern Tibet. Journal of Metamorphic Geology 31, 909–935. http://dx.doi.org/10.1111/jmg.12050.

Weller, O.M., St-Onge, M.R., Searle, M.P., Waters, D.J., Rayner, N., Chen, S., Chung, S.L., Palin, R.M., 2015a. Quantifying the *P–T–t* conditions of north–south Lhasa terrane accretion: new insight into the pre-Himalayan architecture of the Tibetan plateau. Journal of Metamorphic Geology 33, 91–113. http://dx.doi.org/10.1111/jmg.12112.

Weller, O.M., Wallis, S.R., Aoya, M., Nagaya, T., 2015b. Phase equilibria modelling of blueschist and eclogite from the Sanbagawa metamorphic belt of south-west Japan reveals along-strike consistency in tectonothermal architecture. Journal of Metamorphic Geology 33, 579–596. http://dx.doi.org/10.1111/jmg.12134.

White, A.J.R., Smith, R.E., Nadoll, P., Legras, M., 2014. Regional-scale metasomatism in the Fortescue group volcanics, Hamersley Basin, Western Australia: Implications for hydrothermal ore systems. Journal of Petrology 55, 977–1009. http://dx.doi.org/10.1093/petrology/egu013.

White, R.W., Powell, R., Baldwin, J.A., 2008. Calculated phase equilibria involving chemical potentials to investigate the textural evolution of metamorphic rocks. Journal of Metamorphic Geology 26, 181–198. http://dx.doi.org/10.1111/j.1525-1314.2008.00764.x.

White, R.W., Powell, R., Holland, T.J.B., Johnson, T.E., Green, E.C.R., 2014a. New mineral activity–composition relations for thermodynamic calculations in metapelitic systems. Journal of Metamorphic Geology 32, 261–286. http://dx.doi.org/10.1111/jmg.12071.

White, R.W., Powell, R., Johnson, T.E., 2014b. The effect of Mn on mineral stability in metapelites revisited: new a–x relations for manganese-bearing minerals. Journal of Metamorphic Geology 32, 809–828. http://dx.doi.org/10.1111/jmg.12095.

Will, T.M., Schmädicke, E., 2003. Isobaric cooling and anti-clockwise *P–T* paths in the Variscan Odenwald Crystalline Complex, Germany. Journal of Metamorphic Geology 21, 469–480. http://dx.doi.org/10.1046/j.1525-1314.2003.00453.x.

Will, T.M., Lee, S.H., Schmädicke, E., Frimmel, H.E., Okrusch, M., 2015. Variscan terrane boundaries in the Odenwald–Spessart basement, Mid-German Crystalline Zone: new evidence from ocean ridge, intraplate and arc-derived metabasaltic rocks. Lithos 220–223, 23–42. http://dx.doi.org/10.1016/j.lithos.2015.01.018.

Wilke, F.D.H., O'Brien, P.J., Schmidt, A., Ziemann, M.A., 2015. Subduction, peak, and multi-stage exhumation metamorphism: traces from one coesite-bearing eclogite, Tso Morari, western Himalaya. Lithos 231, 77–91. http://dx.doi.org/10.1016/j.lithos.2015.06.007.

Willner, A.P., Massonne, H.J., Krohe, A., 1991. Tectono-thermal evolution of a part of a Variscan magmatic arc: the Odenwald in the Mid-German Crystalline Rise. Geologische Rundschau 80 (2), 369–389. http://dx.doi.org/10.1007/BF01829372.

Worley, B., Powell, R., 2000. High-precision relative thermobarometry: theory and a worked example. Journal of Metamorphic Geology 18, 91–101.

Zhang, H., Li, J., Liu, S., Li, W., Santosh, M., Wang, H., 2012. Spinel + quartz-bearing ultrahigh-temperature granulites from Xumayao, Inner Mongolia Suture Zone, North China Craton: petrology, phase equilibria, and counter-clockwise *P–T* path. Geoscience Frontiers 3, 603–611. http://dx.doi.org/10.1016/j.gsf.2012.01.003.